Modeling Assessment of Spreading of the Scituate Waste Water Treatment Plant in the North-South Rivers, Massachusetts

Changsheng Chen, Liuzhi Zhao, Siqi Li, Huichan Lin

School for Marine Science and Technology
University of Massachusetts-Dartmouth
836 South Rodney French Blvd, New Bedford, MA 02744

Jeff Kennedy, Christian Petitpas, Greg Bettencourt, and Matt Camisa

Massachusetts Division of Marine Fisheries
Shellfish Sanitation and Management Program
706 South Rodney French Blvd, New Bedford, MA 02744

July 5, 2022

Executive Summary

A joint team, the University of Massachusetts-Dartmouth and the Massachusetts Division of Marine Fisheries, applied the unstructured-grid, Finite-Volume Community Ocean Model (FVCOM) to establish a high-resolution (up to ~ 10 m) for the North and South River-intertidal saltmarsh complex. The model was configured with the 1m × 1m resolution LIDAR bathymetry and driven by tidal forcing at the boundary over the inner shelf of the Massachusetts Bay, wind forcing at the surfacing, and the freshwater discharge at the upstream end of the North River. The numerical experiments also considered the 25-, 50-, and 100-year storm wind intensities. Maps were created to project the contaminant coverage area under the seasonally-mean and extreme storm conditions, including spring and neap tidal periods. The model results show that the WWTP contaminated water mainly spread over the Herring River and its surrounding intertidal saltmarsh areas close to New Inlet. The South River is more susceptible to the WWTP contaminant than the North River. Extreme storm winds could expand the contaminated areas over the intertidal saltmarsh but have little influence on the upstream region of the North River and South River. A sensitive analysis was conducted for each season to examine how the contaminant coverage changes in wind direction. The simulation results indicated that the WWTP diluted coverage varied more significantly with wind directions than wind speeds.

1. Introduction and Background

The North and South Rivers are a tidal-dominant estuary connected to Massachusetts By through New Inlet (Fig. 1). This estuary encompasses the extensive intertidal saltmarsh areas, which are flooding and draining almost twice per day. Rapid changes in tidal currents make it a favorite habitat for striped bass, bluefish, and shellfish. Commercial shellfish is a highly valuable industry in Massachusetts. However, due to the lack of assessment of the impact of the Scituate Waste Water Treatment Plant (WWTP) outfall on shellfish habitats, the United State Food and Drug Administration (FDA) infinitely closed shellfish beds on this estuary in 2020. The sewage contains toxic microorganisms. The WWTP effluent could carry these contaminants into the shellfish growing region. In an area with 1000:1 dilution, the toxics could be accumulated in the shellfish body, threading the human health once they enter the fish markets.

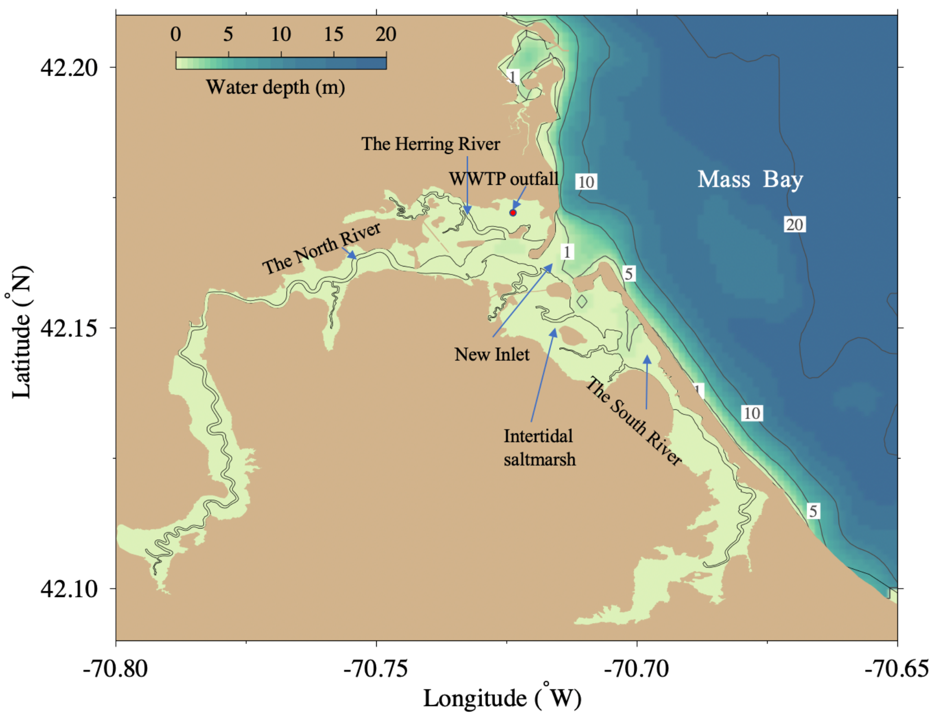

Fig.1. Geometries of the North and South Rivers. The image is the water depth. The light green areas are the intertidal saltmarsh.

Massachusetts Division of Marine Fisheries (MDMF) has criteria to establish the prohibition zones for shellfish harvesting in estuaries and shelves around WWTPs. The 1000:1 dilution serves as a boundary for these zones. The Scituate WWTP discharge exit is located in a shallow mud area connected to a tidal creek of the Herring River, one of the North River tributaries (Fig. 1). The average daily discharge is 1.2 MGD, with a maximum up to 3.3 MGD during the wet weather high flow period. The average peak hourly flow is 2.5 MGD, but the peak hourly wet weather flow can reach 4.0 MGD. The average 95% BOD and SS concentrations are removed from the wastewater at the outfall. Since this estuary features the river-tidal creek-intertidal saltmarsh complex, significantly temporospatial flow variation due to tides and winds makes it challenging to determine dilution boundary empirically using limited observations.

We, the Marine Ecosystem Dynamics Laboratory, School for Marine Science and Technology (SMAST), the University of Massachusetts-Dartmouth (UMASS-D), have established a high-resolution (up to ~10 m) WWTP assessment model for the North and South Rivers by collaborating with the MDMF through a Massachusetts Marine Fisheries Institute (MFI), a cooperative venture between the SMAST/UMASSD and MDMF. The model was developed using the unstructured grid, Finite-Volume Community Ocean Model (FVCOM) (*Chen et al*., 2003, 2006, 2013). One of the most challenging problems in predicting the WWTP effluent spread in the North and South Rivers is to simulate accurately the water transport flooding onto and draining out of the intertidal saltmarsh area and the WWTP effluent dispersion. Since the water exchanges between the main river channel and intertidal saltmarsh go through complex flow movements, including narrow tidal creeks, the model is required to resolve the geometries of these creeks. Failure to do it can lead to an unrealistic dispersion and spreading of the WWTP effluents (Chen et al., 2008). The unstructured triangular grid approach in FVCOM is advantageous for resolving complex estuarine geometry. This model was robust for tracking the discharge of the Yarmouth WWTP in Casco Bay, Maine (True, 2018). We applied it to the Scituate WWTP in Mass Bay, MA, under the high flow condition, including extreme storm scenarios.

This report summarizes the major findings from various numerical model experiments under the seasonal-climatological, 25, 50, and 100-year extreme wind conditions. We also did sensitivity studies to examine the impacts of wind directions and maximum WWTP discharge rates on the spreading and dispersion of the WWTP effluent plume.

The report is organized as follows. Section 2 describes the model, data, and numerical experiment designs. Section 3 manifests the results for the seasonal-climatological, 25, 50, and 500-year extreme storm conditions. Section 4 discusses the sensitivity of the WWTP effluent spreading to wind directions and maximum discharge rates. Section 5 provides the annotations of variables in the model output files. Section 6 summarizes the primary finding, following with suggestions for future works.

2. The Model, Data, and Numerical Experiment Designs

2.1 FVCOM

The Scituate WWTP model assessment model was developed by configuring FVCOM to the North and South Rivers. The FVCOM version used in this trace-tracking experiment employed σ transformation in the vertical and non-overlapping, unstructured triangular grids in the horizontal. The vertical eddy viscosity was produced by the Mellor and Yamada level-2.5 turbulent closure scheme (*Mellor and Yamada*, 1982). The horizontal diffusion coefficients were specified using the Smagorinsky eddy parameterization (*Smagorinsky*, 1961). The FVCOM is solved numerically by a finite-volume flux calculation with the discretization of the integral form of the governing equations at the non-overlapping, unstructured triangular grid node (tracer variables) and centroids (horizontal velocities) (Chen et al., 2003). The triangular grid approach in FVCOM provides the flexibility to make the mesh fit well with irregular coastlines and geometries over the river-tidal creek-intertidal saltmarsh complex. The flux calculation accurately represents the volume mass conservations in individual control volumes for water properties. The discretization, time integration, and coding structure of FVCOM are described in detail in the FVCOM user manual (Chen et al., 2013).

In FVCOM, the primitive equations are advanced in time using either mode-splitting or semi-implicit solvers. This project used the mode-splitting approach in which the two-dimensional (2D barotropic (external) mode was integrated separately from the 3D baroclinic (internal) mode (*Chen et al*., 2003, 2013). The external mode solved the vertically integrated transport equations in which the water elevation was computed explicitly using a shorter time step constrained by min $(l_1, l_2, l_3)\sqrt{gD}$, where $l_1, l_2,$ and l_3 are the three side lengths of the smallest size triangle, g is gravity, D is the total local water depth, and $\sqrt{gD}$ is the local shallow water wave speed. A second-order accurate, fourth-order Runge-Kutta upwind time-stepping scheme was used for flux calculation in the integral form of the advective terms (*Kobayashi et al*., 1999; *Hubbard*, 1999). The internal mode solved fully 3D governing equations using a more extended time step constrained by the phase speed of the lowest mode internal waves (*Chen et a*l., 2003). The linkage between external and internal modes was through the water elevation, and an external-internal mode adjustment was made at each internal time step.

FVCOM simulates the flooding/drying process using unstructured-grid wet/dry point treatment algorithms (*Chen et al*., 2003, 2013, and 2022). Numerical singularity due to a zero depth in the σ-coordinates was avoided by adding a viscous sublayer with a thickness of D_{min} in the equations. The criteria determining the wet or dry in individual grid cells is based on the total water depth at triangle node points and triangular cells. It is given as

$$\begin{cases} wet, & if\ D = H + \zeta - h_B > D_{min} \\ dry, & if\ D = H + \zeta - h_B \le D_{min} \end{cases} \text{, at triangular node points} \tag{1}$$

and

$$\begin{cases} wet, & if\ D = min(-h_{B,\hat{\imath}}, -h_{B,\hat{\jmath}}, -h_{B,\hat{k}}) + max(\zeta_{\hat{\imath}}, \zeta_{\hat{\jmath}}, \zeta_{\hat{k}}) > D_{min} \\ dry, & if\ D = min(-h_{B,\hat{\imath}}, -h_{B,\hat{\jmath}}, -h_{B,\hat{k}}) + max(\zeta_{\hat{\imath}}, \zeta_{\hat{\jmath}}, \zeta_{\hat{k}}) \le D_{min} \end{cases} \text{ at triangular cells} \tag{2}$$

where h_B was the bathymetric height related to the river edge where the mean water depth was zero. $\hat{\imath}$, $\hat{\jmath}$, and $\hat{k}$ were integer numbers to identify the three-node points of a triangular cell. When a triangular cell was treated as dry, the velocity at the centroid of this triangle was specified to be zero, and no flux was allowed through the three side boundaries of this triangle. This triangular cell was removed from the flux calculation in the control volume. A detailed discussion of this unstructured grid wet/dry point treatment technique was given in *Chen et al*. (2003, 2022).

2.2. The North and South River FVCOM (NSR-FVCOM)

The North and South River FVCOM (hereafter referred to as NSR-FVCOM) was developed by configuring FVCOM with the North and South Rivers' bathymetry and external forcings. The computational domain for the NSR-FVCOM covered most areas of these two rivers with cut off inland over the Robinsons Creek Area in North Pembroke, and the North River and the upstream area across Road 3A, Marshfield, the South River (Fig. 2). The open boundary was located in the shelf of Massachusetts Bay with connecting to the Northeast Coastal Ocean Forecast System (NECOFS) grid (Fig. 2). The domain was meshed using a non-overlapping unstructured triangular grid, with the horizontal resolution up to ~10 m in the main river channel and intertidal saltmarsh. It contains a total of 34,382 elements and 17,293 nodes. A uniform sigma coordinate transformation with eleven levels was used in the vertical, corresponding to a vertical resolution of 2.0 m or less over the shelf and 0.5 m or less in the river and intertidal saltmarsh. The 1-m resolution LIDAR bathymetry was used to set up the mean water depth in the NSR-FVCOM. The time step was 0.2 sec for the external mode and the internal-external time step ratio was 4. This ratio was determined based on the stability analysis results (*Chen et al.*, 2022).

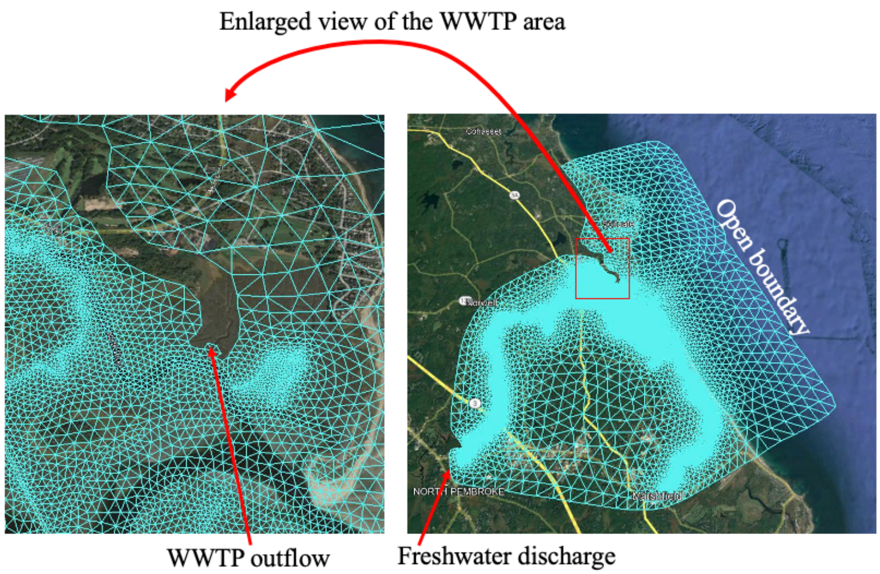

Fig. 2: Right panel: the North and South River (NSR) FVCOM grid. The finest resolution is up to 10 m. Left panel: an enlarged view of the NSR-FVCOM grid around the WWTP outfall area.

2.3 Numerical Experiment Designs

The NSR-FVCOM was driven by the tidal forcing at the open boundaries over the Massachusetts Bay shelf, freshwater discharge at the upstream end of the North River, and winds at the surface. Amplitudes and phases of eight major tidal constituents (M_2, K_2, N_2, S_2, K_1, O_1, P_1, and Q_1) at boundary nodes were specified directly using the output of the NECOFS-predicted tidal elevation. The NECOFS tidal simulation was validated via observation at tidal gauges (*Chen et al*., 2011). The freshwater discharge into the North River varied with season, highest during spring and lowest during autumn. The springtime discharge peak averaged over 2013-2021 was ~170 m^3/s (Fig. 3a).

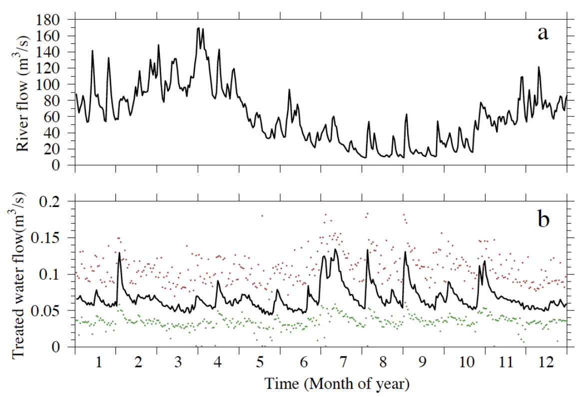

Fig. 3: Upper panel: the daily freshwater discharge entering the North River averaged over 2013-2021. Lower panel: The daily minimum (green dots), averaged (black solid line), and maximum (red dots) WWTP discharges averaged over 2013-2021.

The wind forcing was from the 44-year (1978-2021) hindcast assimilation WRF production of NECOFS. WRF, the Weather Research and Forecasting, is a mesoscale atmosphere model developed by a collaborative group of the National Center for Atmospheric Research (NCAR), the National Centers for Environmental Prediction (NCEP), the U.S. Air Force, the Naval Research Laboratory, the University of Oklahoma, and the Federal Aviation Administration (FAA)

(*Skamarock et al.*, 2008). This model was configured for the U.S. Northeast as a component of NECOFS (*Chen et al*., 2021). The 45-year WRF assimilation results were validated via wind measurements at meteorological buoys available in the region from the Chesapeake Bay to the Nova Scotian shelf, including NOAA buoy#44013 in Mass Bay. The WRF in NECOFS covered the North and South Rivers. A 9-year (2013 to 2021) statistics of the wind speed and direction showed that this area prevailed with northwesterly winds in winter, northwesterly and southwesterly winds in spring, southwesterly in summer, and southwesterly to northwesterly in autumn (Fig. 4). The maximum wind exceeded 12 m/s, a peak of > 16 m/s, occurring in winter, spring, and autumn, even though the occurrence frequency was only in a range of ~2-5%.

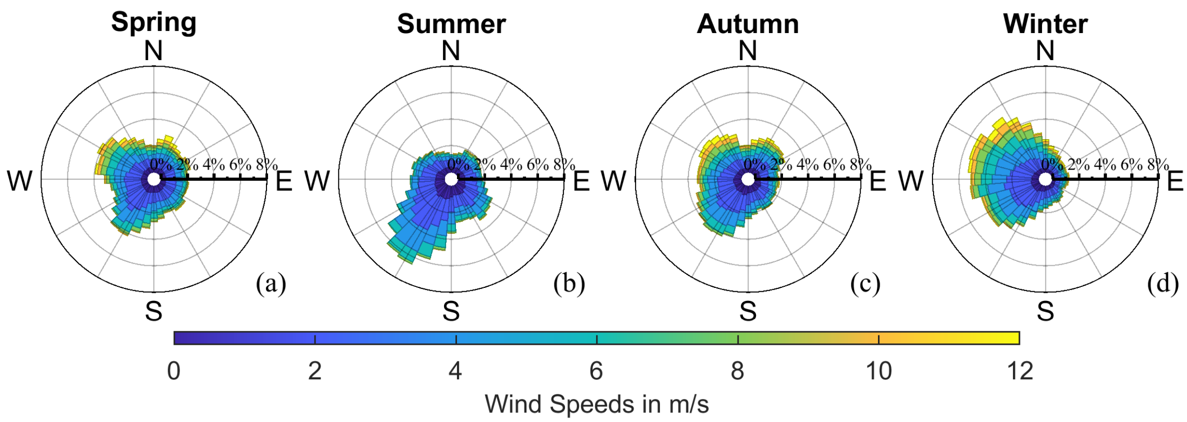

Fig. 4: The wind rose plots for spring, summer, autumn and winter. Colors: wind speed; the circles with percentage labels: the occurrence frequency of the wind. The wind data are from the assimilated NECOFS-WRF hourly output over the North and South Rivers over 2013-2021.

The MDMF has collected the WWTP daily discharges over 2013-2021, including minimum, mean, and maximum values (Fig. 3b). The data format was in MGD, while our input format was m^3/s. The daily discharge in the past nine years generally varied from 0.03 to 0.18 m^3/s, with peaks occurring in summer (June-August). The total daily-averaged discharge changes significantly with time, with a high rate of 0.13 m^3/s during the wet weather high flow period. WWTP discharge was added into the NSR-FVCOM after the tidal currents reached an equilibrium state after a 15-day spin-up.

To estimate the spreading of the WWTP effluents in the North and South Rivers, we designed the numerical experiments by considering first the climatologically seasonal-averaged conditions and then extreme weather and WWTP discharge scenarios. For the climatologically seasonal-averaged cases, the NSR-FVCOM was first to spin up with tidal forcing with freshwater discharges for 15 days and then continued to run for additional 60 days by adding WWTP discharge and wind forcing. The simulation period covered the spring-neap tidal cycles. The results showed that the distribution of the WWTP effluents reached an equilibrium state after 30 days after the WWTP discharge was added, no matter how intense the wind was and in which direction the wind blew from. Since we have no WWTP effluent chemical concentration data, we specified it as 1.0. Therefore, the 1000:1 dilution was defined as a 0.00-contour of the WWTP effluent plume. The climatologically seasonal-averaged forcings were listed in Table 1. To be consistent with the periods of available freshwater and WWTP discharge data, all forcing variables were calculated over the period 2013-2021.

Table 1: Climatologically seasonal-averaged forcings used to drive NSR-FVCOM

Forces / Seasons	Freshwater discharge	WWTP discharge		Wind speed	Wind direction
	m^3/s	m^3/s	MGD	m/s	degree from north
Spring	92.22	0.059	1.354	4.85	284.40
Summer	31.67	0.075	1.703	3.79	209.89
Autumn	39.99	0.072	1.633	5.01	307.11
Winter	81.61	0.064	1.455	5.41	298.65

We considered the extreme weather and WWTP discharge conditions in the WWTP dilution simulations. The model was forced by the 25, 50, and 100-year storm winds for the extreme weather cases. The National Institute of Standards and Technology (NIST) developed an extreme wind speed excel software that can determine the return period of the extreme wind for given historical wind records (http: www.itl.nist.gov/div898/winds/excel.htm). We input the 43-year (1978 to 2021) wind records into this software and estimated the maximum winds of the 25, 50, and 100-year storms swept in the North and South Rivers (Table 2). The wind speed under extreme weather conditions could exceed 20 m/s, 4-5 times stronger than the climatologically seasonal-averaged wind speed.

Table 2: the 25, 50, and 100-year storm wind speeds

Return period (year)	Wind speed (m/s)
25	23.92
50	25.60
100	27.27

We ran the model by adding the maximum discharge rates recorded in each season over 2013-2021 for extreme WWTP discharge cases. The excessive discharge rate exceeded 0.18 m^3/s in spring through autumn and reached 0.15 m^3/s in winter (Table 3).

Table 3: Seasonal-maximum WWTP discharges

Season	WWTP discharge (m3/s)
Spring	0.180
Summer	0.183
Autumn	0.182
Winter	0.150

.

Over the North and South River areas, the wind direction varied significantly with time. In addition to seasonal climatology, we also examined the sensitivity of the WWTP effluent dilution to the changes in the wind direction by running the NSR-FVCOM with northeasterly, southeasterly, southwesterly, and northwesterly winds. This sensitivity experiment was done for the climatological and extreme storm conditions.

3. Model Results

3.1. Climatologically seasonal-mean WWTP discharges

Under the seasonally-averaged forcing conditions, a large portion of the WWTP effluents is advected out to the shelf through New Inlet, accounting for ~84-85%. The contaminants diluted rapidly over the shelf, and the covered area bounded by a 1000:1 dilution contour is smaller or comparable over the shelf than inside the estuary (Table 4). If we define the area bounded by a 1000:1 dilution contour as polluted, the model results suggest that extreme storm winds change the contaminant retention and coverage area. For example, with the seasonal-mean WWTP discharge, the ratio of the inside to the total polluted areas under a 100-year storm condition was decreased by ~14.5, 2.5, 3.2, and 10.2% in spring, summer, autumn, and winter. Correspondingly, the polluted area inside the estuary reduced by 35.3, 59.7, and 26.7% in spring, summer, and winter (Fig. 5). During the autumn, the 50- and 100-year storm winds tend to retain about 6.2-10.1% more contaminant inside the estuary (Fig. 5). During the winter and spring, the polluted coverage area could reach approximately a steady state after the wind intensity is stronger than the 25-year storm wind. During autumn, the area reaches a maximum at the 50-year storm wind but decreases under a 100-year storm condition. The winter is the only season that the polluted area shows a monotonous decrease as the wind intensity increases.

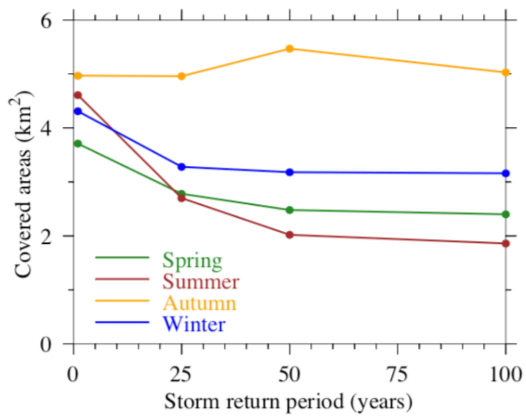

Fig. 5: the change of the covered area of the WWTP contaminants inside the estuary. The estimation was made for the area bounded by the 1000:1 dilution contour.

Table 4: The spreading areas bounded by the 1000:1 dilution contour. Total: the total coverage area; inside: the coverage area in the estuary bordered by the New Inlet exit to the shelf; %: the percentage of the inside to the total.

Cases	Spring			Summer			Autumn			Winter		
	Total (km^2)	Inside (km^2)	%	Total (km^2)	Inside (km^2)	%	Total (km^2)	Inside (km^2)	%	Total (km^2)	Inside (km^2)	%
Seasonally-mean	5.67	3.71	65.47	9.99	4.61	46.16	8.32	4.97	59.78	6.69	4.31	64.42
25-y storm	5.20	2.78	53.34	5.19	2.70	52.04	7.77	4.96	63.86	5.65	3.38	58.04
50-y storm	4.89	2.48	50.72	4.61	2.02	43.90	8.78	5.47	62.29	5.73	3.18	55.56
100-y storm	4.71	2.40	50.96	4.26	1.86	43.70	8.90	5.03	56.55	5.82	3.16	54.27

The spatial distribution of the high concentration WWTP effluents inside the estuary remains relatively stable during all the seasons. Most of these effluents are advected to the upstream area of the Herring River and spread over the intertidal saltmarsh (Fig. 6). The 1000:1 dilution line varied significantly with the season. The most influential regions are located in New Inlet and a portion of the South River connected to the inlet. No model results indicate that the WWTP contaminated water can enter the North River, ~0.5 km away from the WWTP outfall.

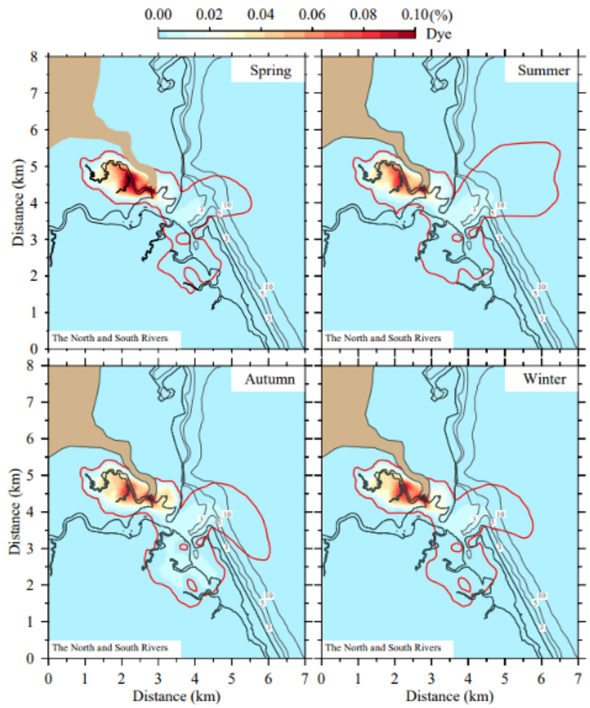

Fig. 6: Distributions of the WWTP effluents under the spring, summer, autumn, and winter climatologically-mean conditions.

These seasonal distribution patterns remain unchanged during the spring and neap tidal periods, but the covered area bounded by the 1000:1 dilution line significantly differs. During the spring tidal period, at high tide, this ratio line could expand to a place of 0.8, 1.5, 1.4, and 0.7 km away from the WWTP outfall in the North River during spring, summer, autumn, and winter (Fig. 7: left panels). Meanwhile, the influenced area of the 1000:1 dilution line shifts inland onto the intertidal saltmarsh over the South River area during all the seasons.

At low tide, the WWTP effluents are tended to be significantly washed out to the shelf. The distribution of the contaminant concentration over the Herring River-intertidal saltmarsh complex remains the same as that at high tide, but the maximum concentration is slightly lower. The influence of the WWTP contaminated water on the North River was considerably lower at low tide, but the area expanded over the intertidal saltmarsh zone connected to the South River. Although the high tide during the spring tidal cycle shows the most significant influence of the WWTP contaminated water on the North and South Rivers' estuary, the maximum influence area is within a 4.0 km ×4.0 km area from the outfall.

During the neap tidal period, a large portion of the WWTP contaminant can accumulate around the outfall area and in the Herring River on the left of the outfall. At high tide, the worst condition over the South River-intertidal saltmarsh complex occurs in autumn, while the impact of the WWTP effluents on the North River is minimal, especially in the area ~1.0 km away from the WWTP outfall. The condition in spring and winter is better than in summer and autumn. At low tide, the influence of the WWTP effluents on the North and South Rivers remains similar to the high tide condition. The most significant difference is in New Inlet, which shows a more extensive outflow transport to the shelf during the low tide.

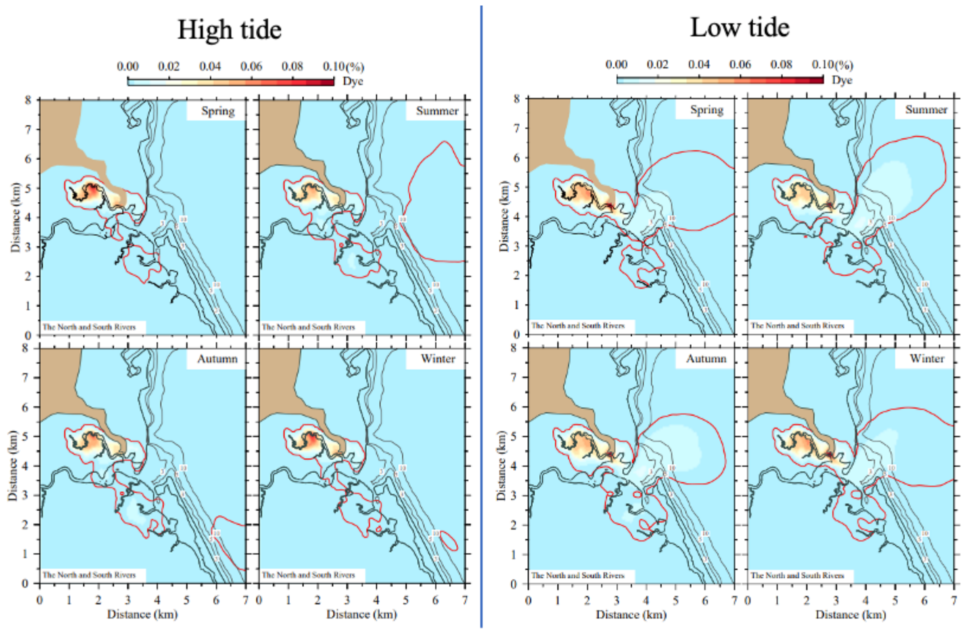

Fig. 7: Distributions of the WWTP effluents during the spring tidal period under the spring, summer, autumn, and winter climatologically-mean conditions. Left panels: high tide; right panels: low tide.

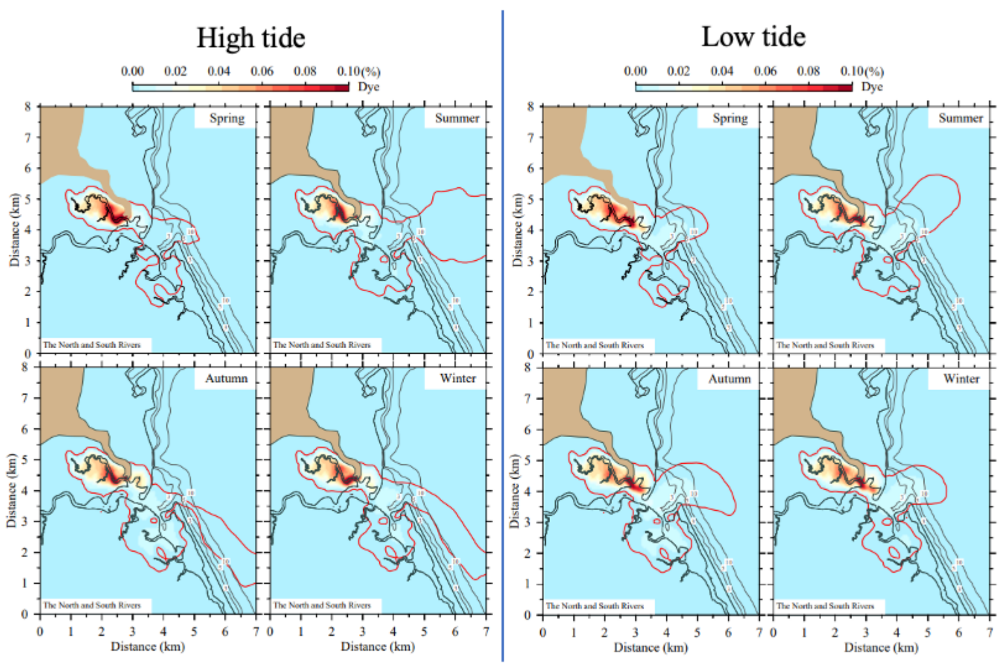

Fig. 8: Distributions of the WWTP effluents during the neap tidal period under the spring, summer, autumn, and winter climatologically-mean conditions. Left panels: high tide; right panels: low tide.

3.2. Seasonal maximum WWTP discharges

Under the seasonally-mean physical forcing conditions, increasing the WWTP discharge rate does not significantly change the covered areas of the WWTP contaminated water bounded by a 1000:1 ratio contour inside the estuary, even though the concentration in the Herring River-intertidal saltmarsh areas dramatically increases (Fig. 9). Similar results are also found during the

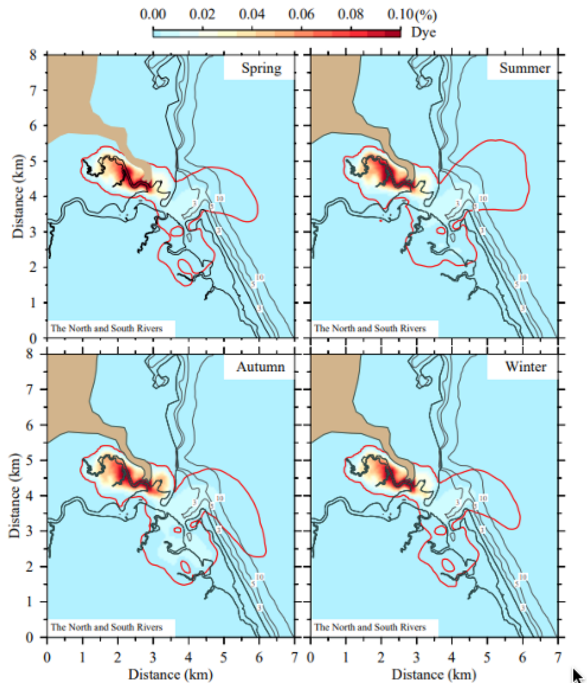

Fig. 9: Distributions of the WWTP effluents under the seasonal-maximum discharge conditions in spring, summer, autumn, and winter.

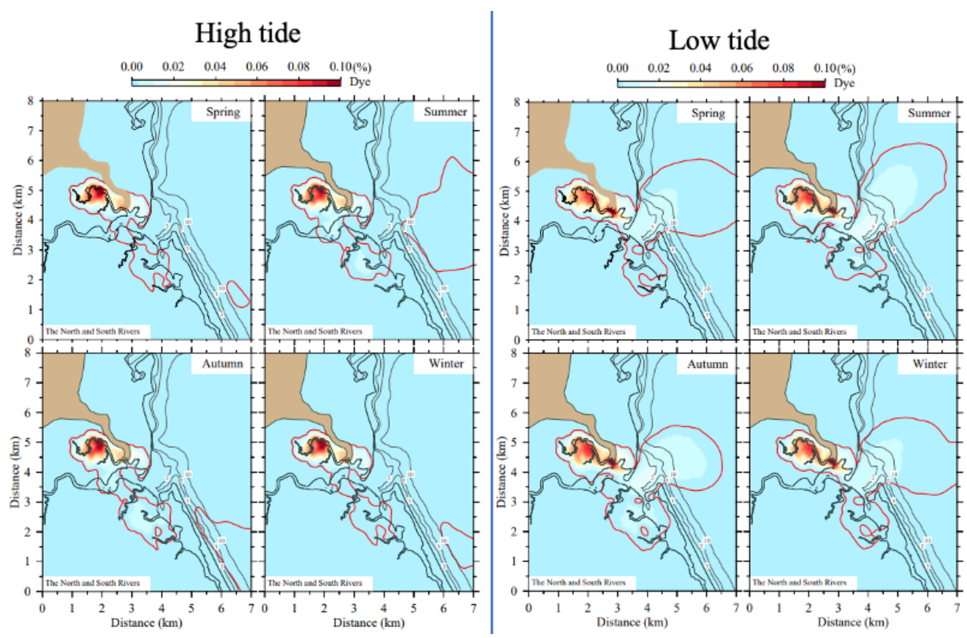

Fig. 10: Distributions of the WWTP effluents during the spring tidal period under the seasonal maximum WWT discharge in spring, summer, autumn, and winter. Left panels: high tide; right panels: low tide.

spring (Fig. 10) and neap (Fig.11) tidal periods. The WWTP discharge rate could affect the contaminant concentration within the covered area of the WWTP effluents. The tidal current intensity can change the covered area of the WWTP contaminated water bounded by a 1000:1 dilution line, but this covered area seems not to be significantly influenced by the WWTP discharge rate.

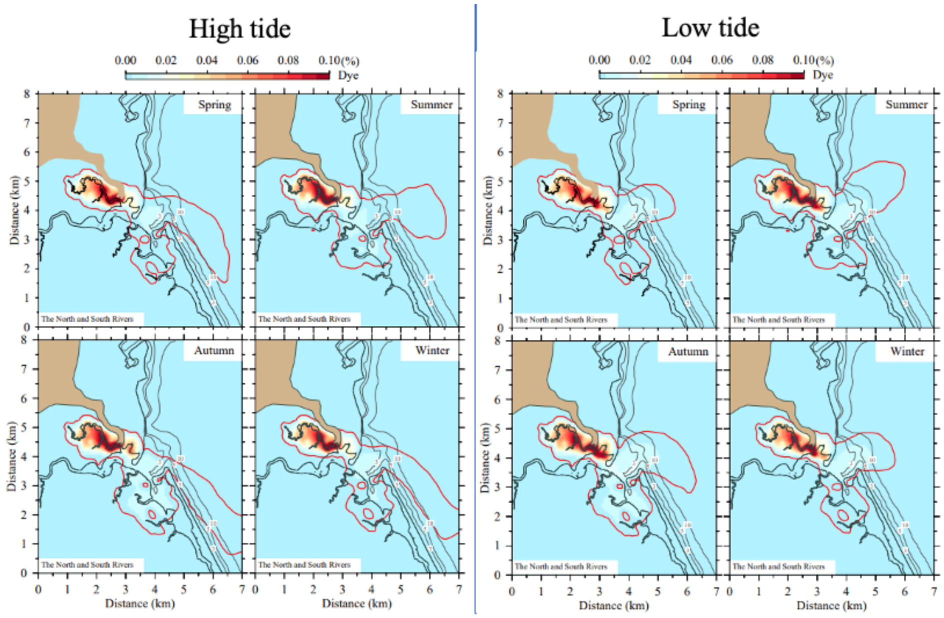

Fig. 11: Distributions of the WWTP effluents during the neap tidal period under the seasonal maximum WWT discharge in spring, summer, autumn, and winter. Left panels: high tide; right panels: low tide.

3.3. Extreme storm winds

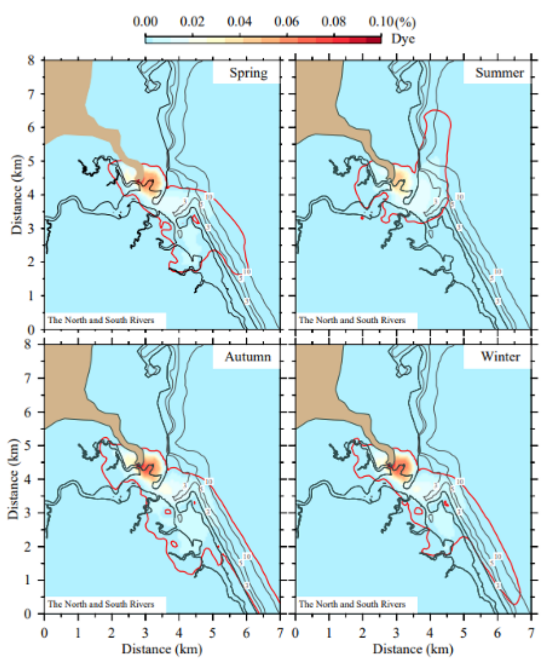

Fig. 12: Distributions of the WWTP effluents under seasonal-maximum discharge conditions in spring, summer, autumn, and winter for the case with the 100-year storm winds.

We have traced the WWTP effluents by driving the NSR-FVCOM with the 25, 50, and 100-year storm winds in spring, summer, autumn, and winter. The model was run with the seasonally-mean and seasonal-maximum WWTP discharges. The distributions and spreading areas of the WWTP contaminated water bounded by a 1000:1 dilution contour for all these cases are shown in the figures in Appendix-A and Appendix-B. For example, the 100-year storm wind cases with the seasonal-maximum WWTP discharge are presented here.

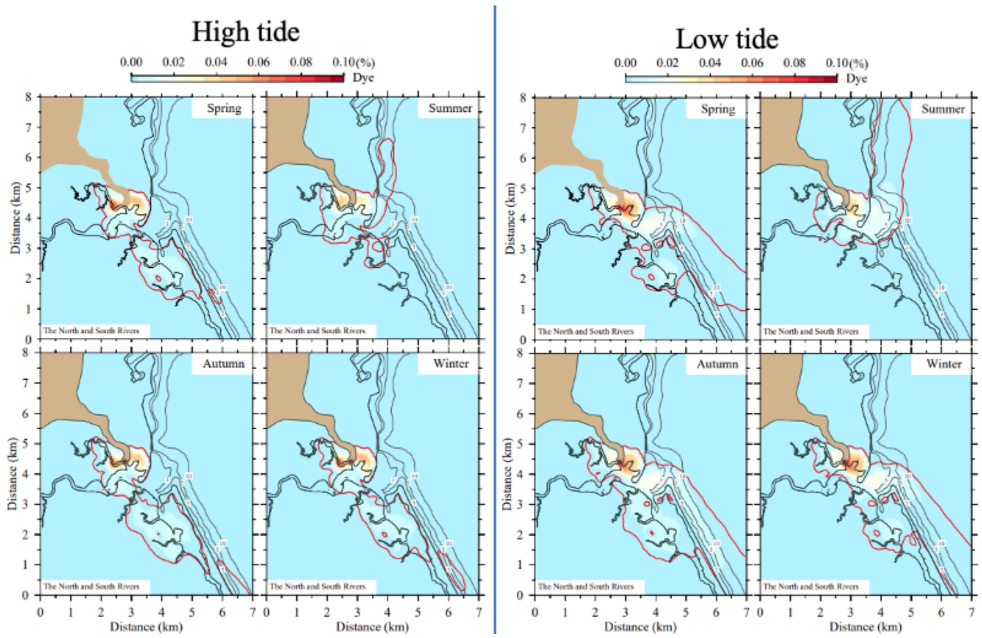

Fig. 13: Distributions of the WWTP effluents during the spring tidal period under the seasonal maximum WWT discharge in spring, summer, autumn, and winter for the case with the 100-year storm winds. Left panels: high tide; right panels: low tide.

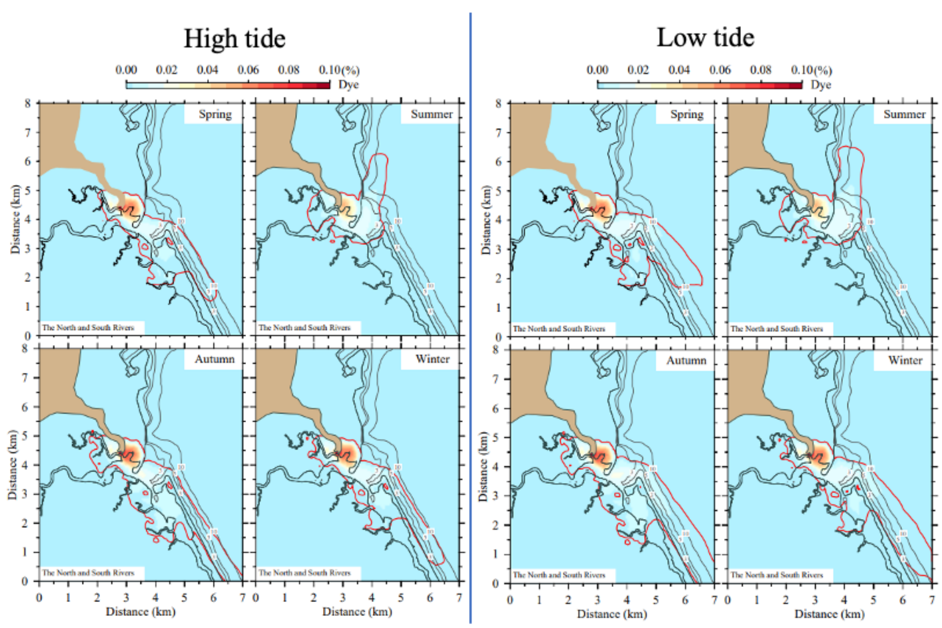

Fig. 14: Distributions of the WWTP effluents during the neap tidal period under the seasonal maximum WWT discharge in spring, summer, autumn, and winter for the case with the 100-year storm winds. Left panels: high tide; right panels: low tide.

Compared with the WWTP effluent distributions shown in Fig. 9, the strong wind enhanced the outflow water transport from the Herring River to the shelf through New Inlet. The wind can reduce the contaminant concentration over the Herring River-intertidal saltmarsh complex, with its maximum trapped around the WWT outfall (Fig. 12). Meanwhile, the 1000:1 ratio concentration contour can expand inland in the North River area, but such an expansion mainly over the intertidal saltmarsh areas. During summer, the enhanced washout from New Inlet to the shelf can limit the contaminant transport to the South River, reducing the pollution risk in that area.

As aforementioned, the tidal intensity plays a crucial role in expanding the spreading area of the WWTP contaminated water in this estuary. The maximum spreading toward the main channel of the North River occurs at high tide during the spring tidal period. This feature does not change in the case of 100-year storm winds. Compared with the seasonally-mean wind case shown in Fig. 10, the strong storm wind could slightly expand the 1000:1 ratio line southward, especially during summer (Fig. 13). Meanwhile, the enhanced southwesterly wind during the summer can help reduce the flux of the WWTP contaminant into the South River (Fig. 13). The distributions of the WWTP contaminated water during the neap tidal period are similar to the seasonally mean condition shown in Fig. 12 (Fig. 14). For all these cases, the South River is more susceptible to the WWTP contaminant than the North River.

3.4. Sensitivity to wind directions

We have examined the changes in the spatial distribution of the WWTP effluents with wind directions for all experiment cases, including the seasonal-mean and extreme storm wind scenarios with seasonal-mean and maximum WWTP discharges. The sensitivity analysis results show that the spreading distribution of the WWTP contaminant varies with wind direction. An example is shown in Figs. 15-16 for the 100-year storm wind case with seasonal-maximum WWTP discharges. In the North River area, the widest spreading occurs during a northeasterly wind condition. In the South River area, the worst situation is during a northwesterly wind condition.

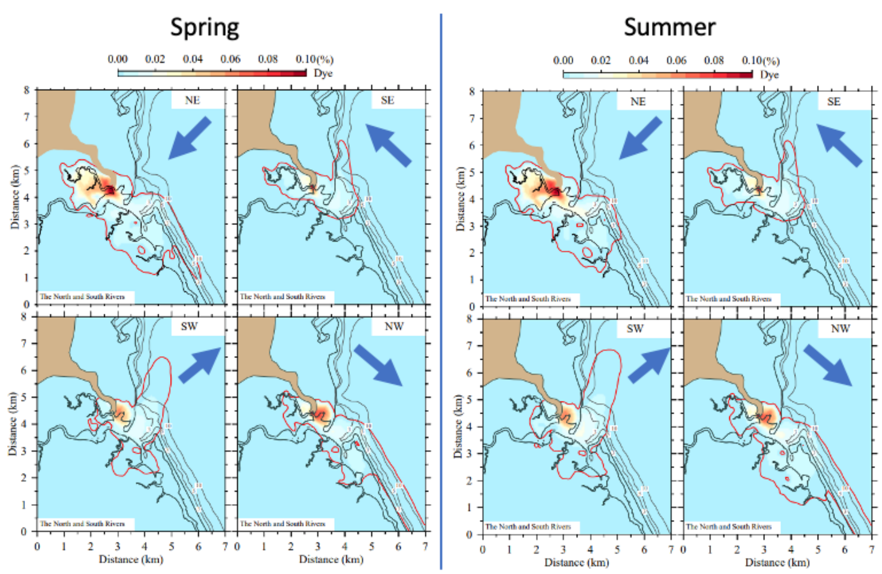

Fig. 15. Distributions of the WWTP effluents at high tide during the spring tidal period under the seasonal maximax WWT discharge in spring and summer for the case with the 100-year storm winds. Arrows indicate the direction the wind blows.

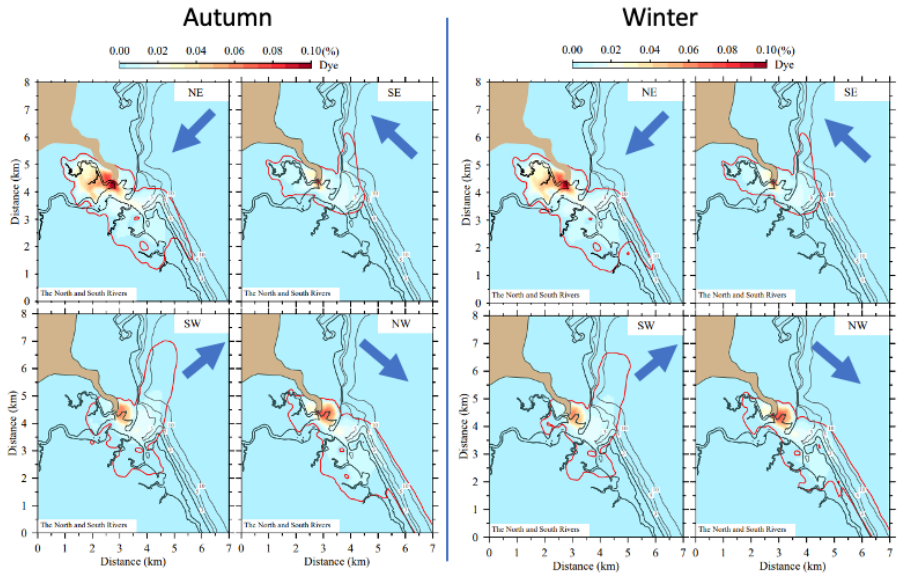

Fig. 16. Distributions of the WWTP effluents at high tide during the spring tidal period under the seasonal maximum WWT discharge in autumn and winter for the case with the 100-year storm winds. Arrows indicate the direction the wind blows.

4. Maximum covered areas of the WWTP contaminant

We have created the maps showing the maximum spreading areas of the WWTP contaminant with a concentration of 1000:1 or higher for each season. Two types of maps were created. One offers the maximum coverage of the WWTP contaminant under the seasonally-mean wind conditions. Another includes the impacts of 25, 50, and 100-year storm winds. In each map, the

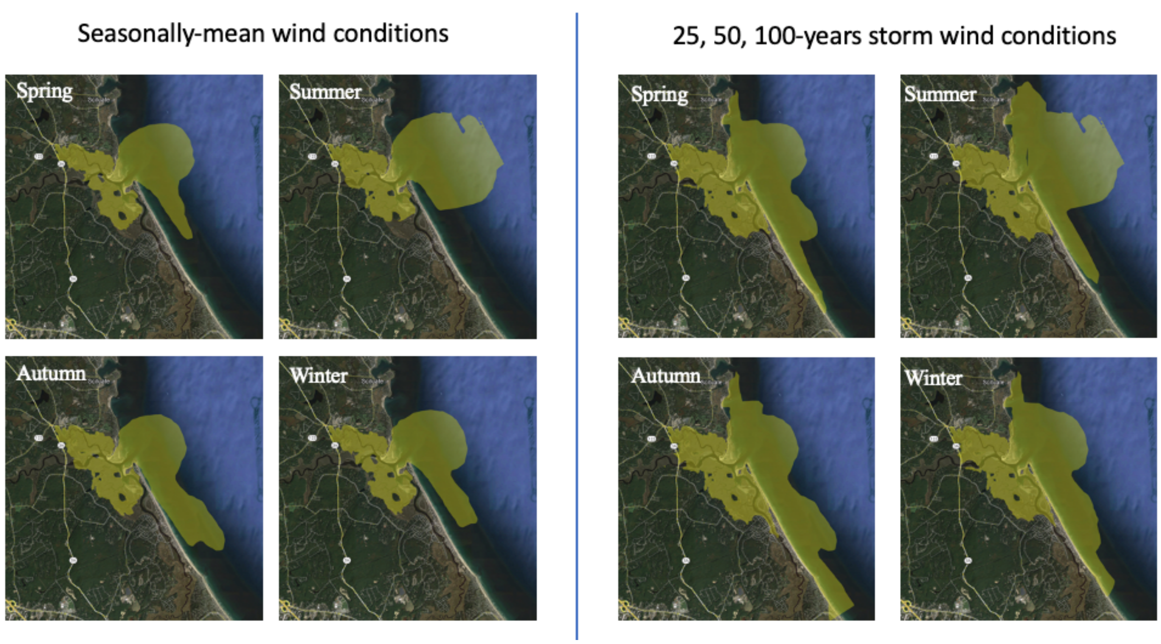

Fig. 17. The maximum coverages of the WWTP contaminant with a concentration of 1000:1 or higher under the seasonal-mean wind (left panels) and extreme storm wind (right panel) conditions for four seasons. All cases took the seasonal-mean and maximum WWTP discharges into accounts. The simulations includes the spring and neap tidal cycles.

results were from the ensemble experiments considering the seasonal-mean and maximum WWTP discharges and the changes in the wind direction rotating over 360°. Maps also account for the influence of spring and neap tidal current variation. The map for the seasonal-mean wind condition presents a general environment during each season (Fig. 17: left panels). The maps considering the extreme storm wind project what maximum spreading could occur during a storm event (Fig. 17: right panels).

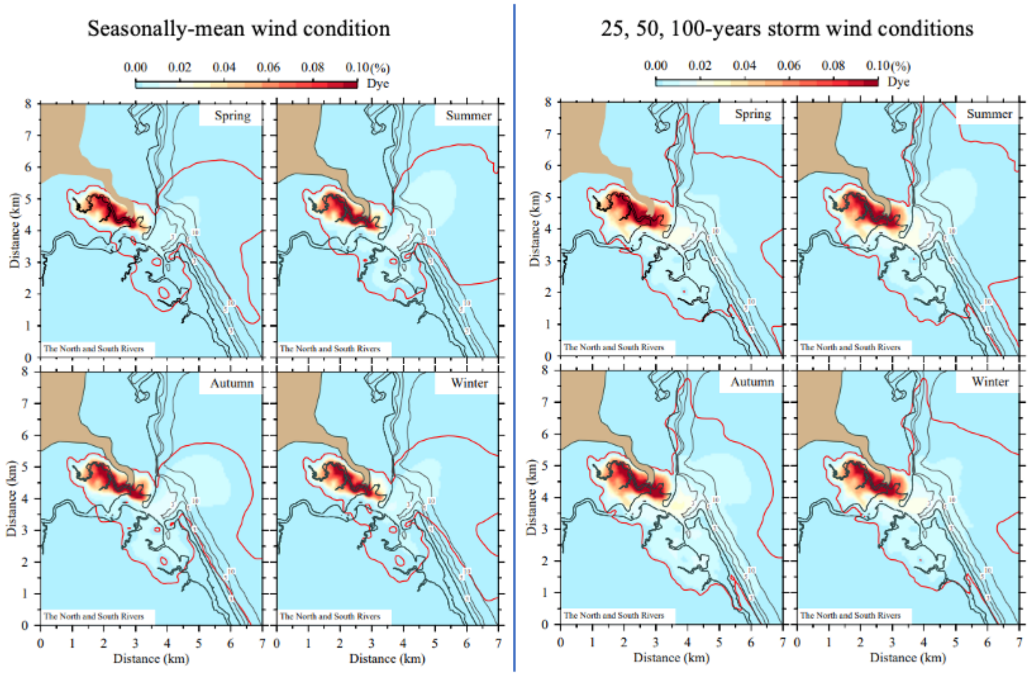

Fig. 18. The enlarged views of the maximum coverages of the WWTP contaminant with a concentration of 1000:1 or higher under the seasonal-mean wind (left panels) and extreme storm wind (right panel) conditions for four seasons. All cases took the seasonal-mean and maximum WWTP discharges into accounts. The simulations includes the spring and neap tidal cycles.

Under the seasonal-mean wind conditions, the influences of the WWTP are mainly over the intertidal saltmarsh and river areas around the New Inlet (Fig. 18: left panels). Even at high tide during the spring tidal period, the contaminants are hard to move further into the North and South Rivers a few kilometers away from the WWTP outfall. The extreme storm wind could expand the influence area westward to the North River and southward to the South River (Fig. 18: right panels). These two maps provide a view of the short-term (storm period) and long-term (seasonal) impact of the WWTP effluents on the region.

Although the WWTP contaminants could cover a broad area around New Inlet, the high concentration contaminants mainly stay over the Herring River-intertidal saltmarsh complex. In other areas, the concentration is generally lower than 0.02 (Fig. 18). This condition remains unchanged during the extreme storm wind period, even though the covered area could be much broader. It should be noted that the map showing the extreme storm wind conditions only presents the worst situation that probably could occur occasionally.

5. Summary and Suggestions

A high-resolution (up to ~ 10 m) NSR-FVCOM was developed and applied to assess the impact of the Scituate WWTP outfall on the local shellfish environment in the North and South Rivers. Numerical experiments were done considering seasonal-mean and maximum WWTP discharges under the seasonal-mean, 25, 50, and 100-year storm wind conditions. The simulation period covers the spring-neap tidal cycles. The maximum spreading coverage maps of the WWTP contaminants were created for seasonal-mean and extreme storm wind scenarios. The simulation results show that the high-concentration contaminants mainly remain over the Herring River-intertidal saltmarsh areas. Although the contaminant concentration is relatively low in other areas, the areas bounded by the 1000:1 ratio concentration could cover a broad area, especially in the area connected to New Inlet in the South River. The contaminant coverage area varies significantly with tidal current intensity and wind direction. These changes differ in the North and South Rivers.

Maps showing the maximum coverage of the WWTP contaminants with the 1000:1 dilution or higher present the worst conditions under the seasonal-mean and extreme wind conditions. These worst scenarios could occur in the North River at high tide during the spring tidal period and in the South River during both spring and the neap tidal periods.

The significant variability of the WWTP spreading due to wind directions suggests that we should transfer the existing NSR-FVCOM to establish a forecast model system. This system could provide a scientific tool to monitor and predict the temporospatial variation of the WWTP effluents in this estuary. The Marine Ecosystem Dynamics Modeling Laboratory has already established a Northeast Coastal Ocean Forecast System (NECOFS) in the region. It is straightforward to add the NSR-FVCOM into NECOFS.

References

Chen, C., H. Liu, and R.C. Beardsley, 2003. An unstructured grid, finite-volume, three-dimensional, primitive equation ocean model: application to coastal ocean and estuaries, *J. Atmos. Oceanic Technol.*, 20, 159-186.

Chen, C., R. C. Beardsley, and G. Cowles, 2006. An unstructured grid, finite-volume coastal ocean model (FVCOM) system. Special Issue entitled “Advance in Computational Oceanography,” *Oceanography*, vol. 19, No. 1, 78-89.

Chen, C., J. Qi, C. Li, R. C. Beardsley, H. Lin, R. Walker, and K. Gates, 2008. Complexity of the flooding/drying process in an estuarine tidal-creek salt-marsh system: an application of FVCOM. Journal of Geophysical Research-Oceans, 113, C07052doi: 10.1029/ 2007jc004328.

Chen, C., H. Huang, R. C. Beardsley, Q. Xu, R. Limeburner, G. W. Cowles, Y. Sun, J. Qi, and H. Lin, 2011. Tidal dynamics in the Gulf of Maine and New England Shelf: An application of FVCOM. Journal of Geophysical Research-Oceans, 116, C12010, doi:10.1029 /2011JC007054.

Chen, C., R. C. Beardsley, G. Cowles, J. Qi, Z. Lai, G. Gao, D. Stuebe, H. Liu, Q. Xu, P. Xue, J. Ge, R. Ji, S. Hu, R. Tian, H. Huang, L. Wu, H. Lin, Y. Sun, L. Zhao (2013a), An unstructured-grid, finite-volume community ocean model FVCOM user manual (3rd edition), *SMAST/UMASSD Technical Report-13-0701*, University of Massachusetts-Dartmouth, pp 404.

Chen, C., Z. Lin, R. C. Beardsley, T. Shyka, Y, Zhang, Q. Xu, J. Qi, H. Lin, and D. Xu, 2021. Impacts of sea level rise on future storm-induced coastal inundations over Massachusetts coast. Natural Hazard, https://doi.org/10.1007/s11069-020-04467-x.

Chen, C., J. Qi, J., H. Liu, R. C. Beardsley, H. Lin, G. Cowles, G, 2022. A wet/dry point treatment method of FVCOM, Part I: stability experiments. *J. Mar. Sci. Eng*., 10, 896. https://doi.org/10.3390/jmse10070896

Mellor, G.L., and T. Yamada, 1982. Development of a turbulence closure model for geophysical fluid problem, *Rev. Geophys. Space. Phys*., 20, 851-875.

Smagorinsky, J., 1963. General circulation experiments with the primitive equations, I. The basic experiment. *Mon. Wea. Rev.*, 91, 99-164.

True, E. D.2018. Using a Numerical Model to Track the Discharge of a Wastewater Treatment Plant in a Tidal Estuary. Water, Air, & Soil Pollution, 229(8), 267.

Appendix A: The Distributions of WWTP effluents for the cases under 25, 50, and 100-year storm wind conditions

This appendix includes figures showing the distributions of WWTP contaminated waters for the cases under 25, 50, and 100-year storm wind conditions. The explanation is described in the caption of each figure.

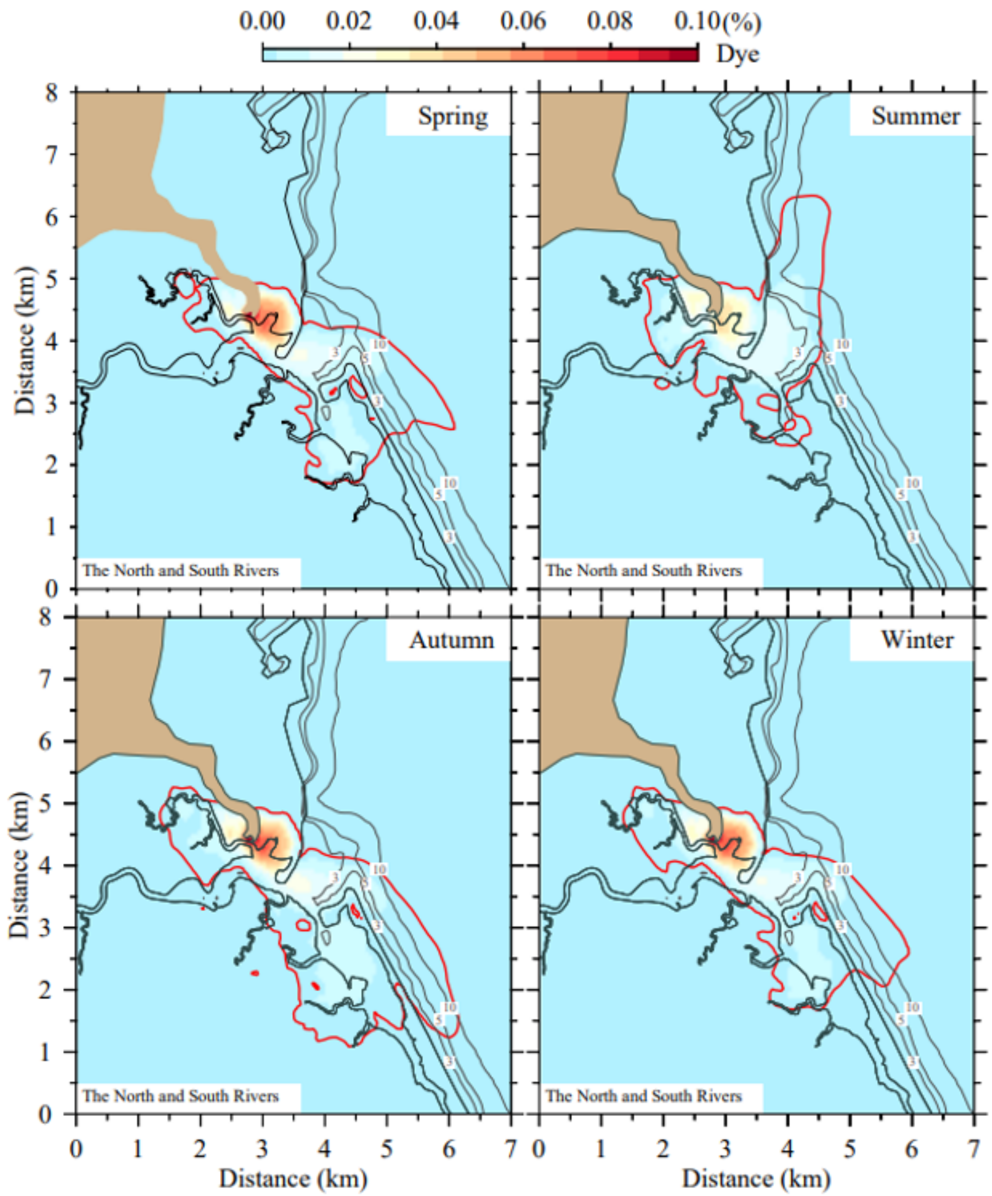

Fig. A1: Tidal-averaged distributions of the WWTP effluents under seasonal-mean discharge conditions during spring, summer, autumn, and winter for the case with the 25-year storm winds.

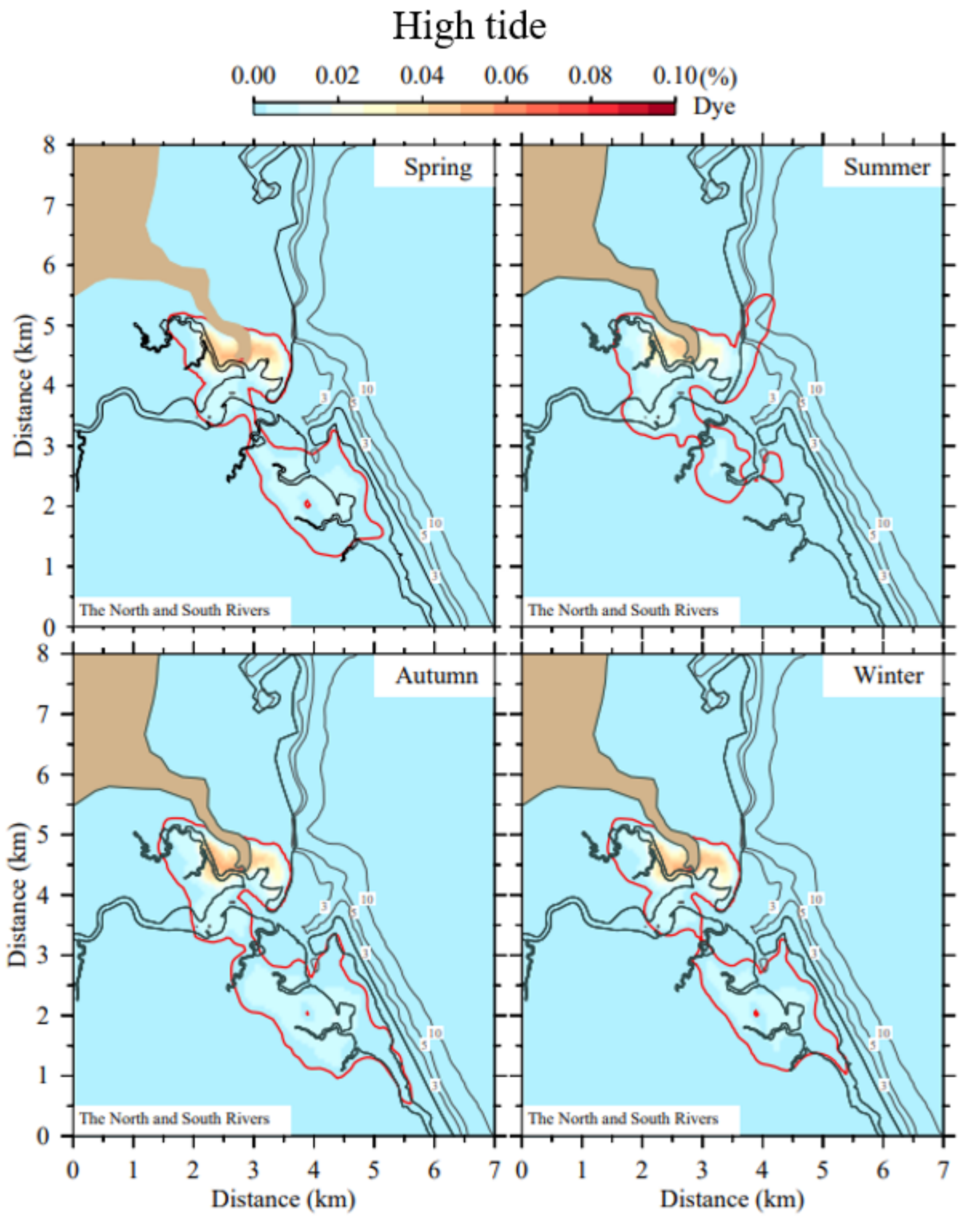

Fig. A2: Distributions of the WWTP effluents at high tide during the spring tidal period under seasonal-mean discharge conditions during spring, summer, autumn, and winter for the case with the 25-year storm winds.

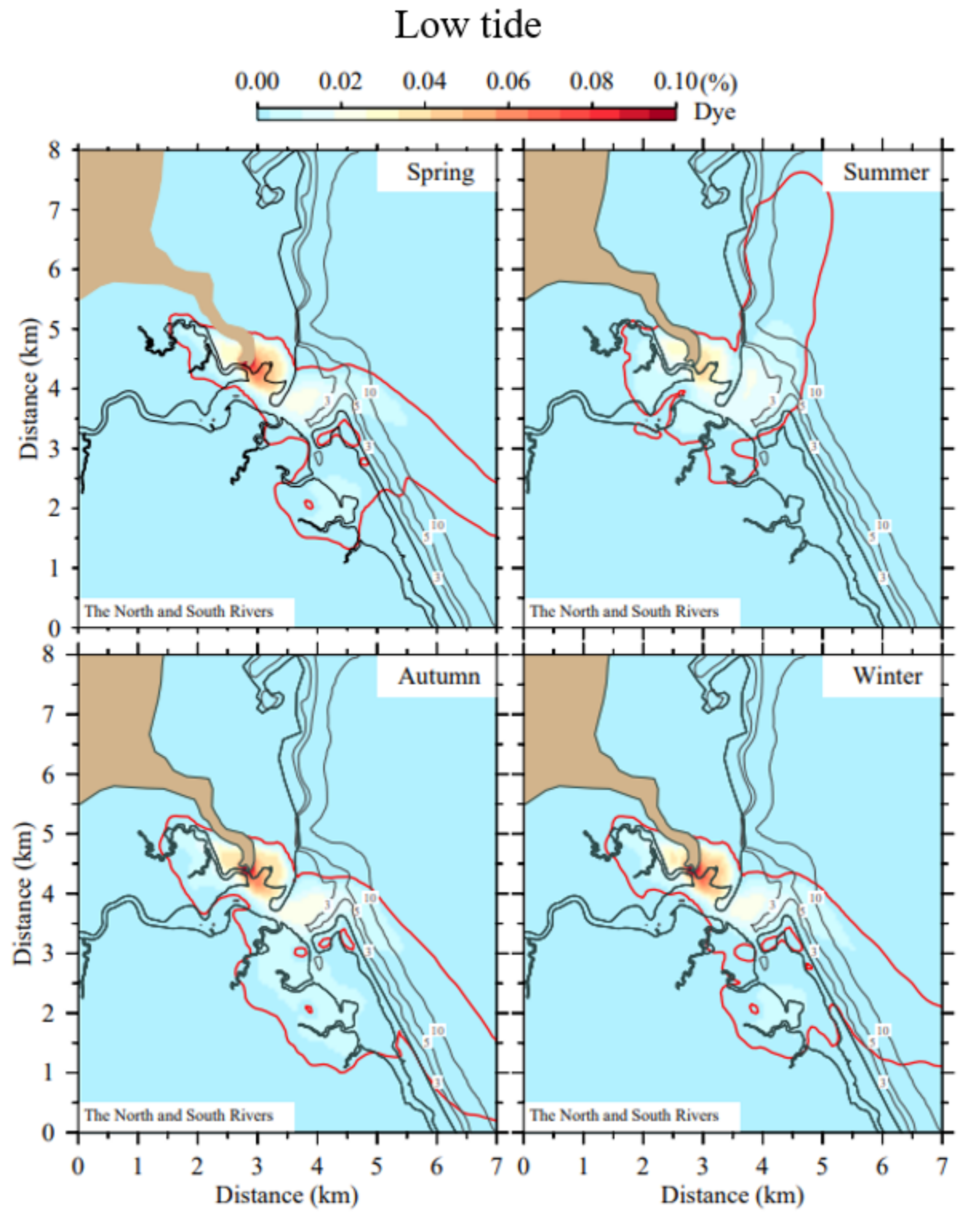

Fig. A3: Distributions of the WWTP effluents at low tide during the spring tidal period under seasonal-mean WWT discharge conditions during spring, summer, autumn, and winter for the case with the 25-year storm winds.

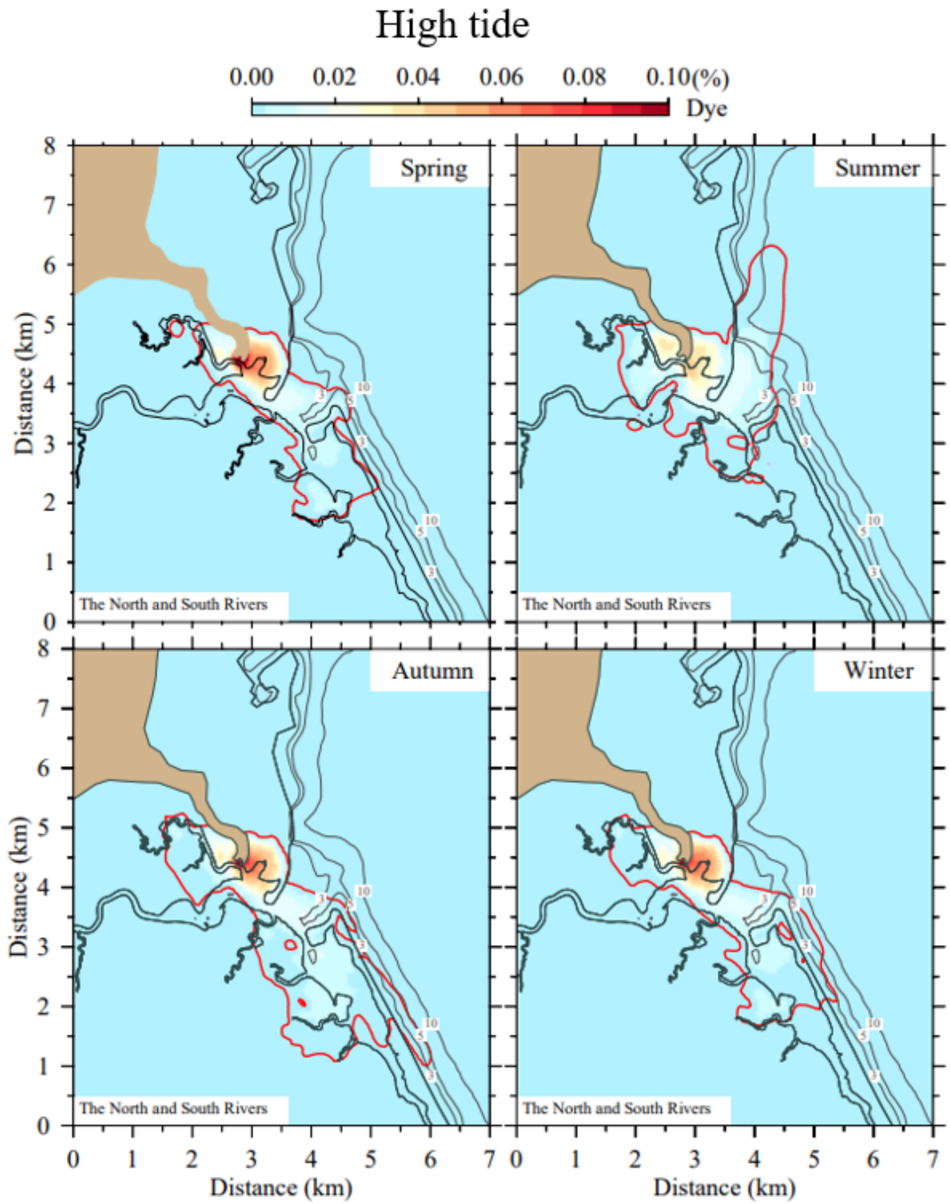

Fig. A4: Distributions of the WWTP effluents at high tide during the neap tidal period under seasonal-mean WWT discharge conditions in spring, summer, autumn, and winter for the case with the 25-year storm winds.

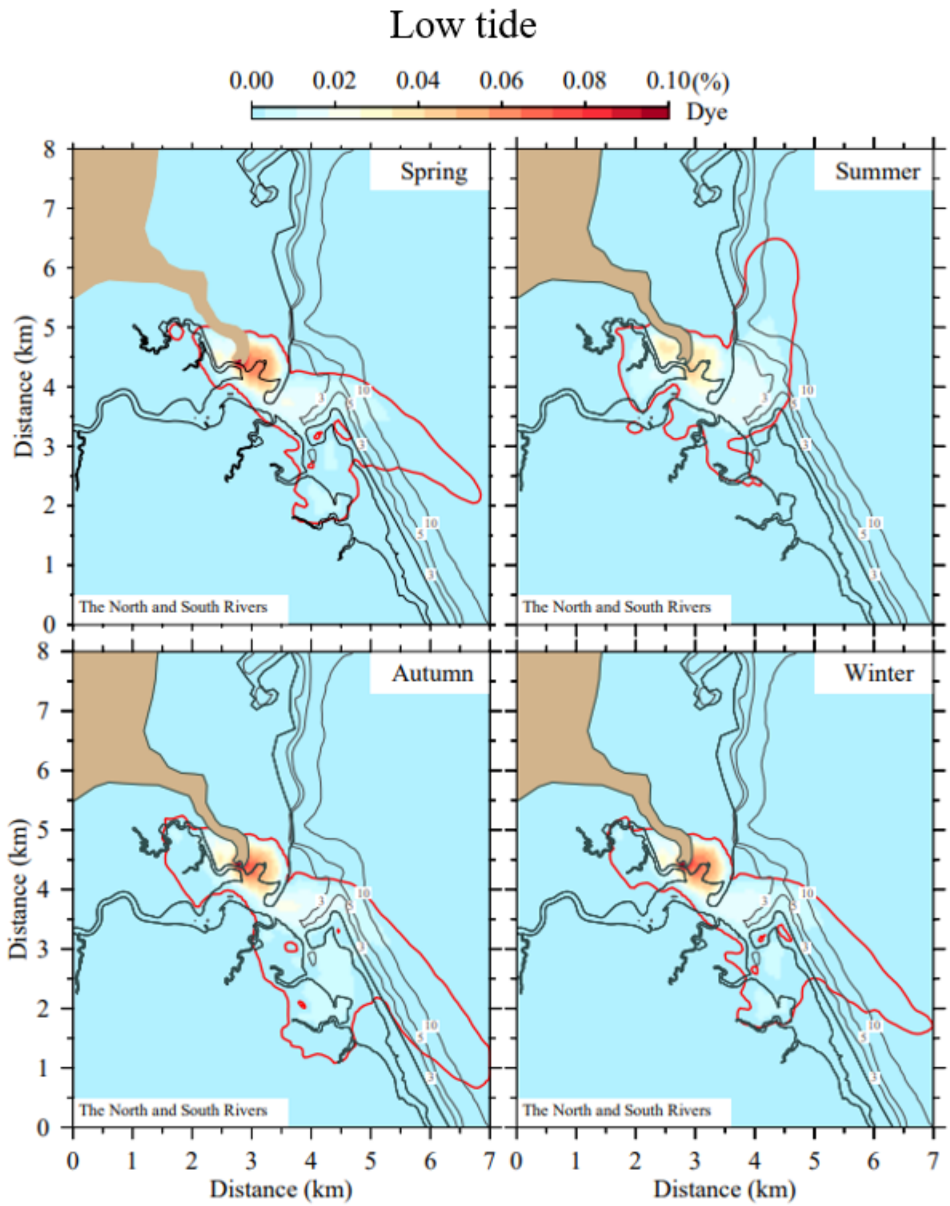

Fig. A5: Distributions of the WWTP effluents at low tide during the neap tidal period under seasonal-mean WWT discharge conditions during spring, summer, autumn, and winter for the case with the 25-year storm winds.

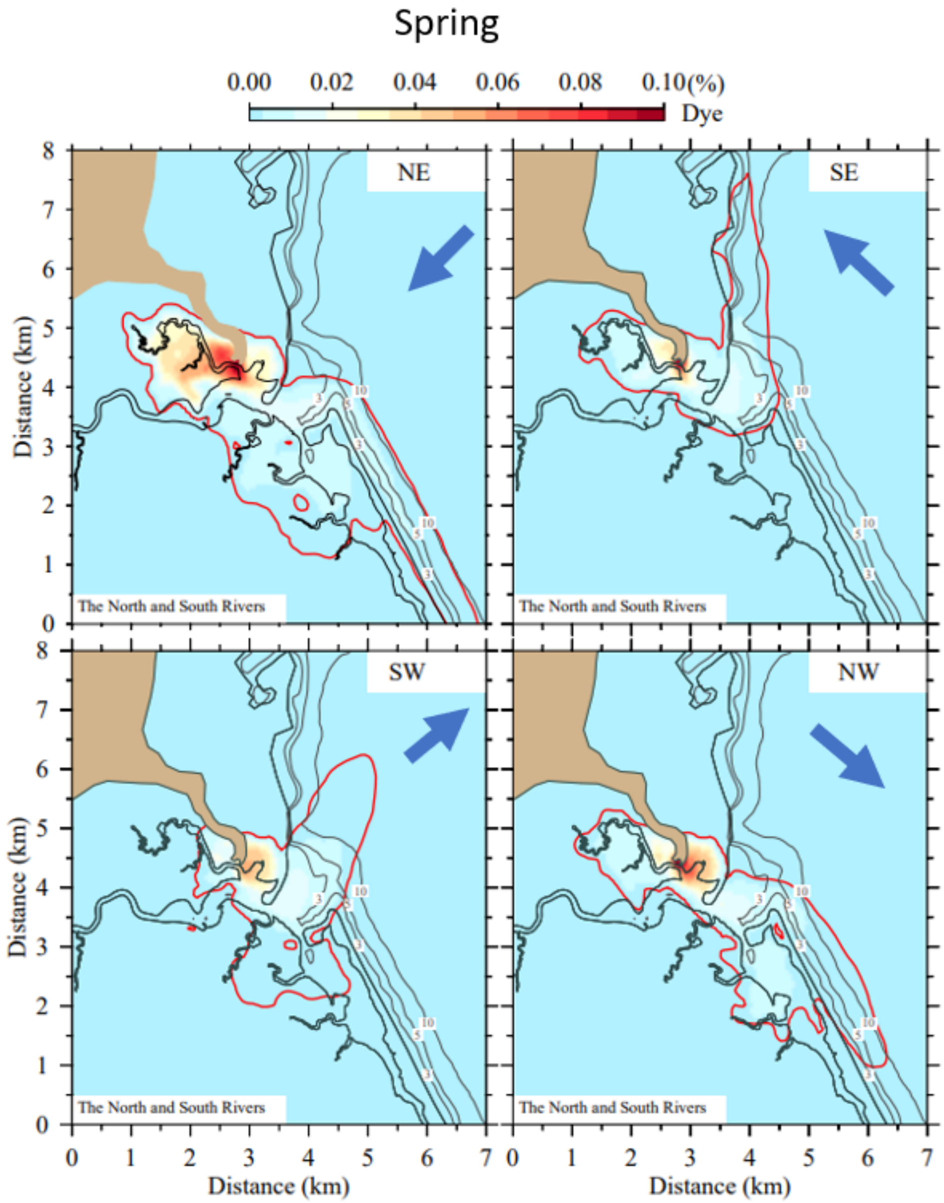

Fig. A6: Distributions of the WWTP effluents at high tide during the spring tidal period under northeasterly (NE), southeasterly (SE), southwesterly (SW), and northwesterly wind conditions. The model was run with seasonal-mean WWTP discharge in spring under a 25-year storm wind condition for spring. Arrows indicate the wind directions.

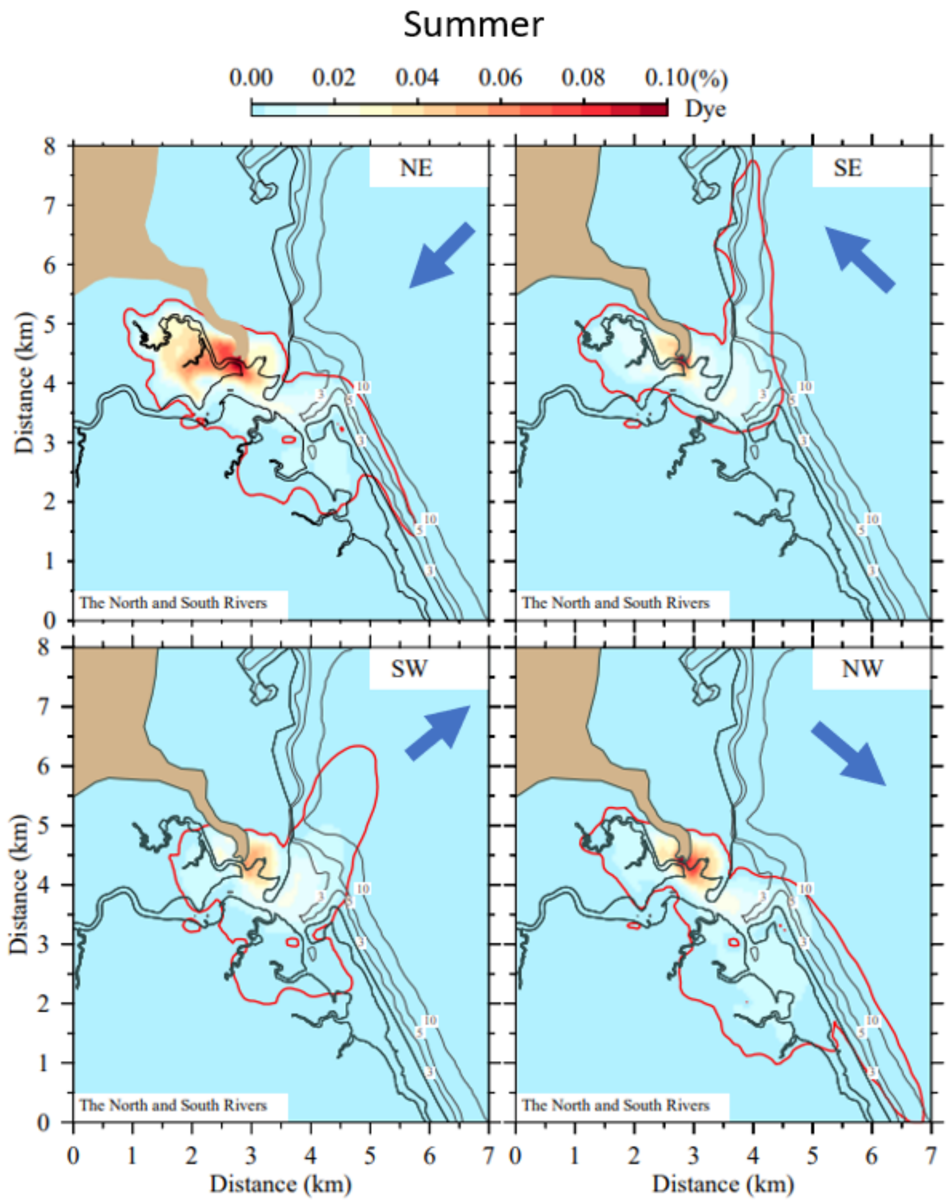

Fig. A7: Distributions of the WWTP effluents at high tide during the spring tidal period under northeasterly (NE), southeasterly (SE), southwesterly (SW), and northwesterly wind conditions. The model was run with seasonal-mean WWTP discharge in spring under a 25-year storm wind condition for summer. Arrows indicate the wind directions.

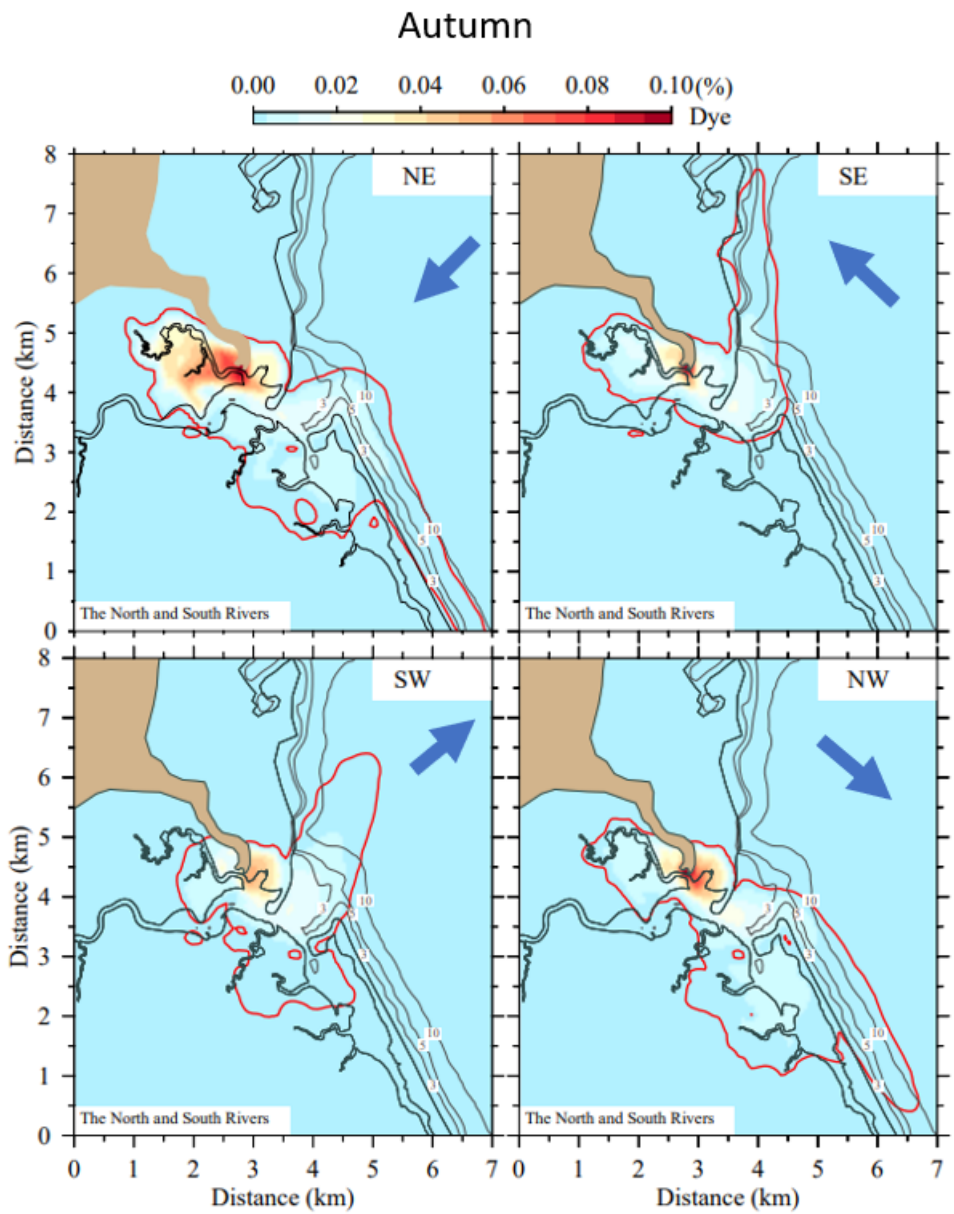

Fig. A8: Distributions of the WWTP effluents at high tide during the spring tidal period under northeasterly (NE), southeasterly (SE), southwesterly (SW), and northwesterly wind conditions. The model was run with seasonal-mean WWTP discharge in spring under a 25-year storm wind condition for autumn. Arrows indicate the wind directions.

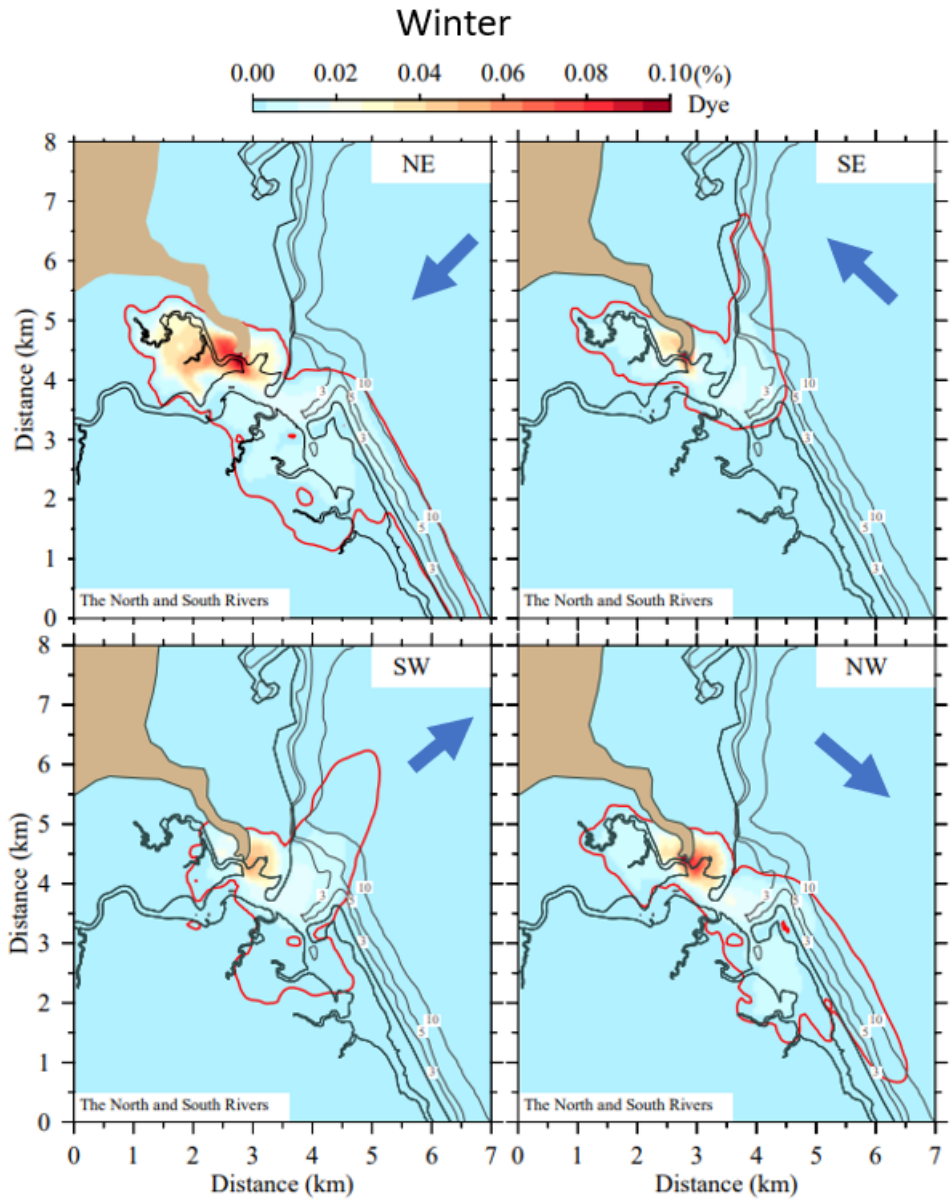

Fig. A9: Distributions of the WWTP effluents at high tide during the spring tidal period under northeasterly (NE), southeasterly (SE), southwesterly (SW), and northwesterly wind conditions. The model was run with seasonal-mean WWTP discharge in spring under a 25-year storm wind condition for winter. Arrows indicate the wind directions.

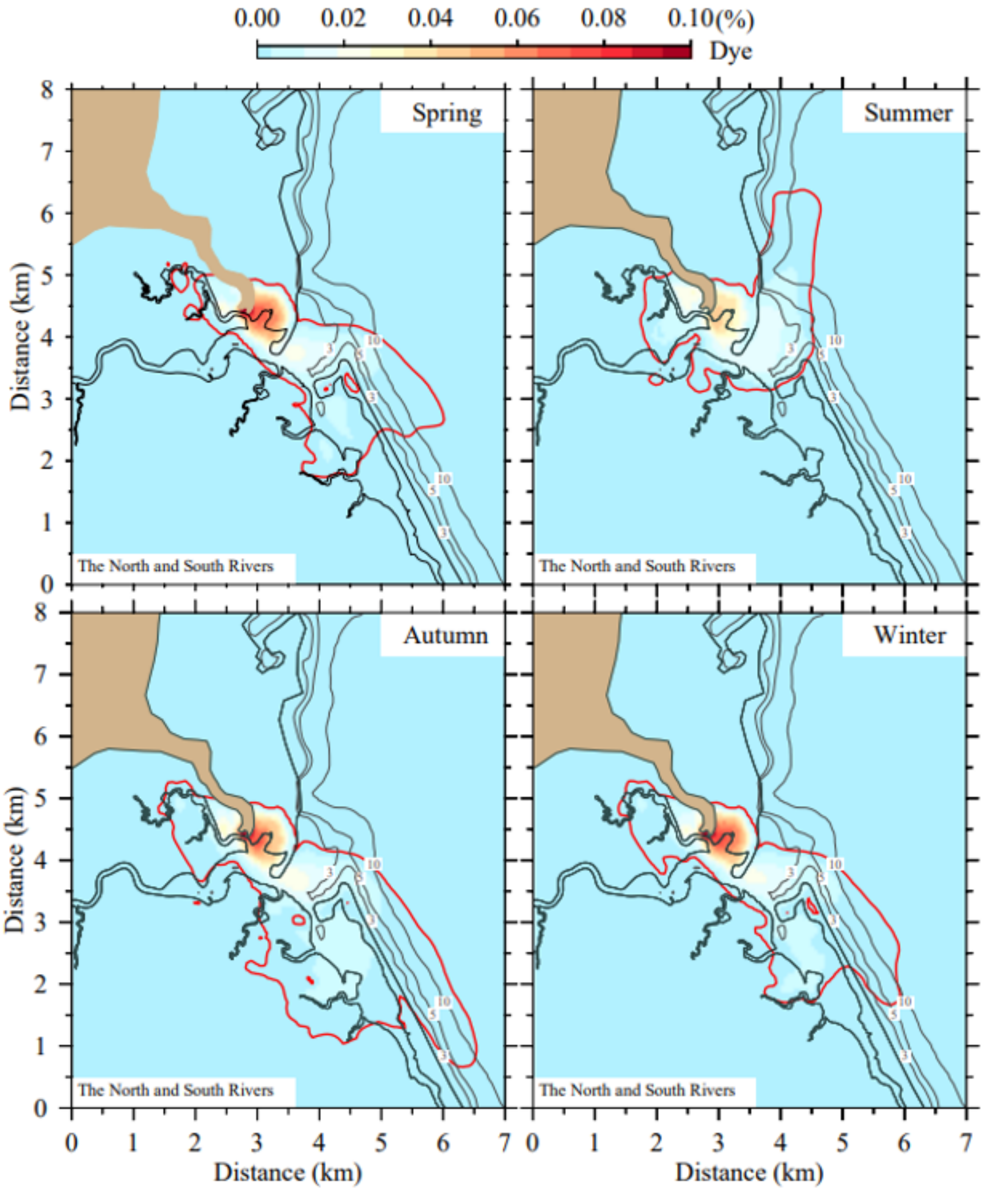

Fig. A10: Tidal-averaged distributions of the WWTP effluents under seasonal-mean discharge conditions during spring, summer, autumn, and winter for the case with the 50-year storm winds.

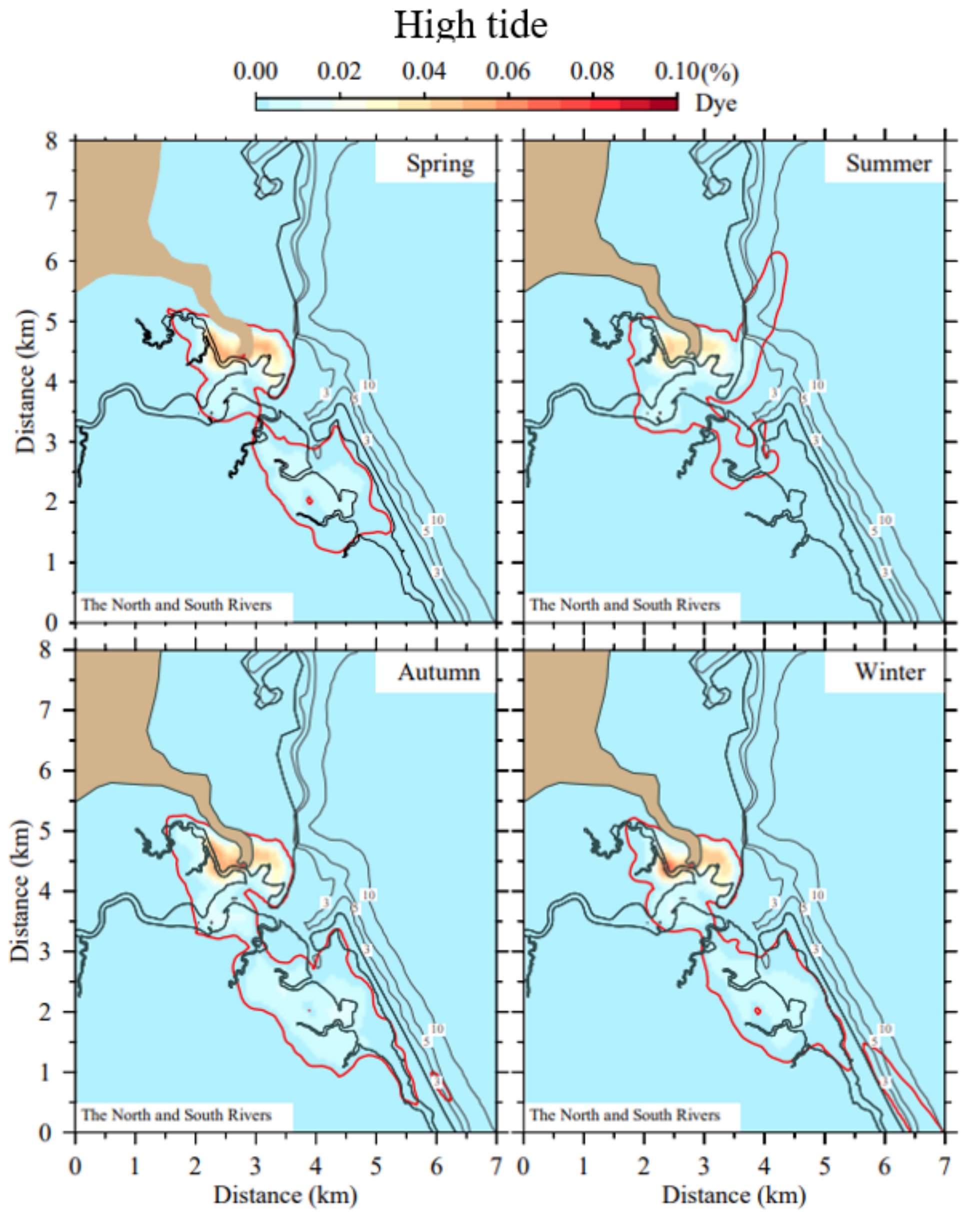

Fig. A11: Distributions of the WWTP effluents at high tide during the spring tidal period under seasonal-mean discharge conditions during spring, summer, autumn, and winter for the case with the 50-year storm winds.

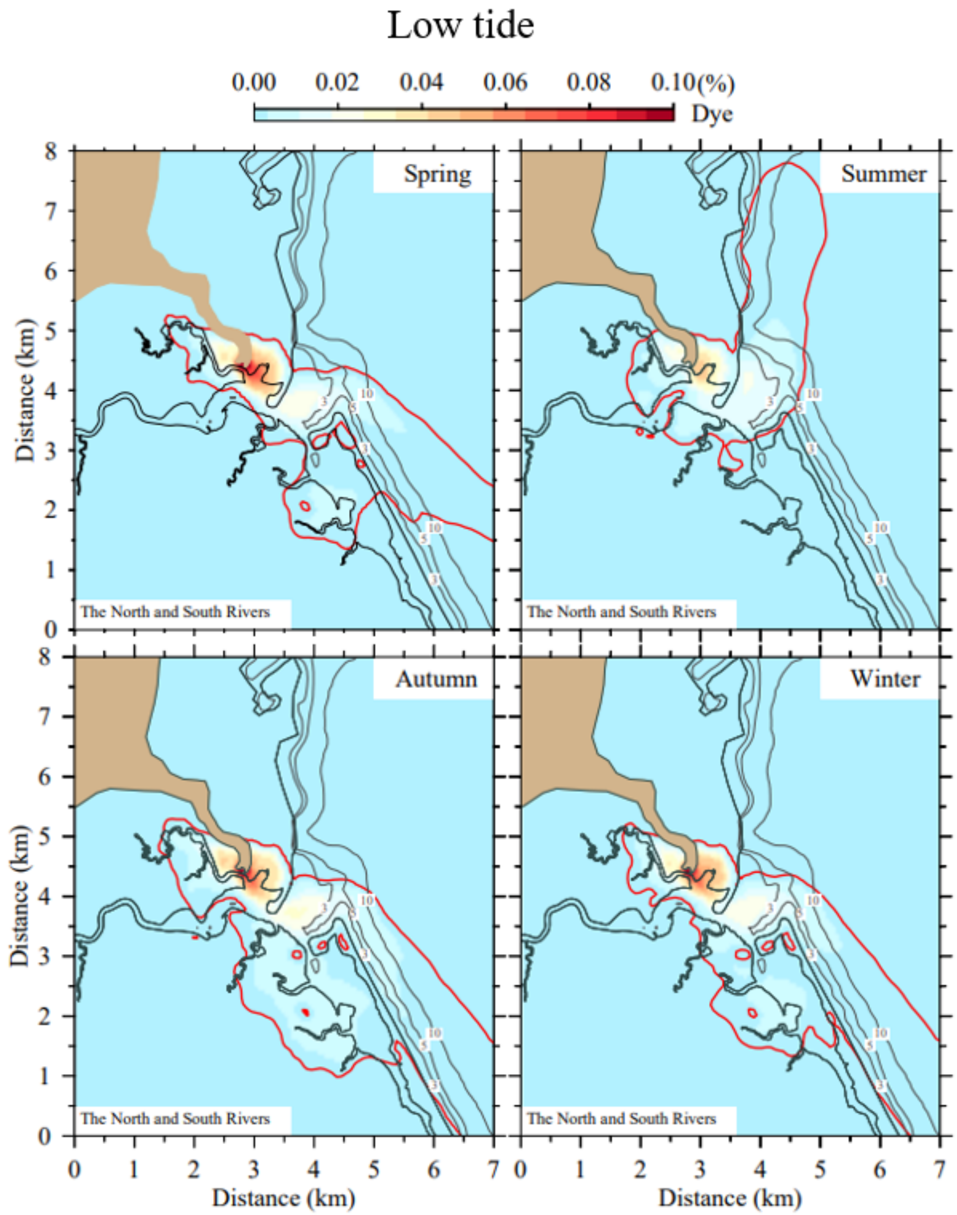

Fig. A12: Distributions of the WWTP effluents at low tide during the spring tidal period under seasonal-mean discharge conditions during spring, summer, autumn, and winter for the case with the 50-year storm winds.

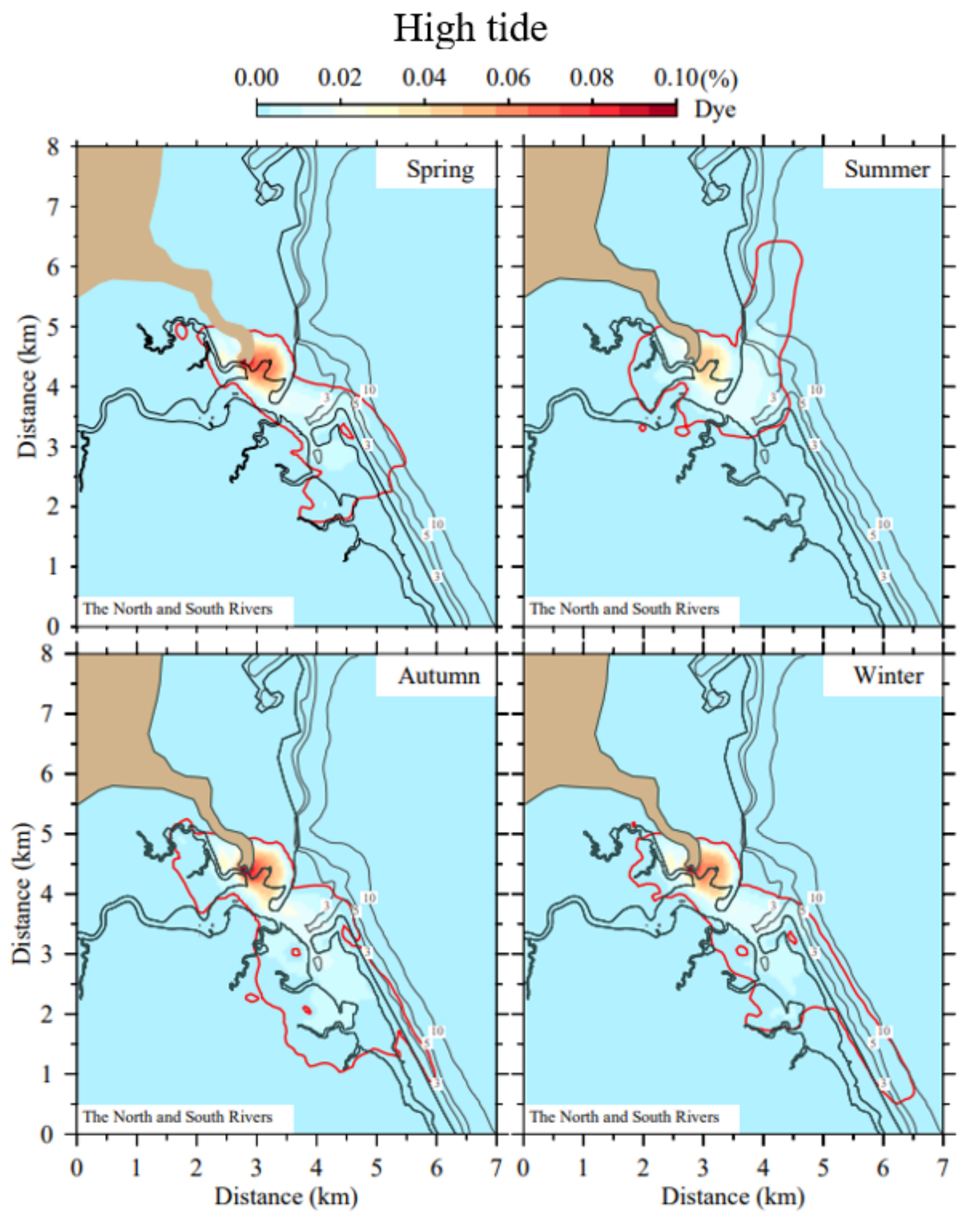

Fig. A13: Distributions of the WWTP effluents at high tide during the neap tidal period under seasonal-mean WWT discharge conditions in spring, summer, autumn, and winter for the case with the 50-year storm winds.

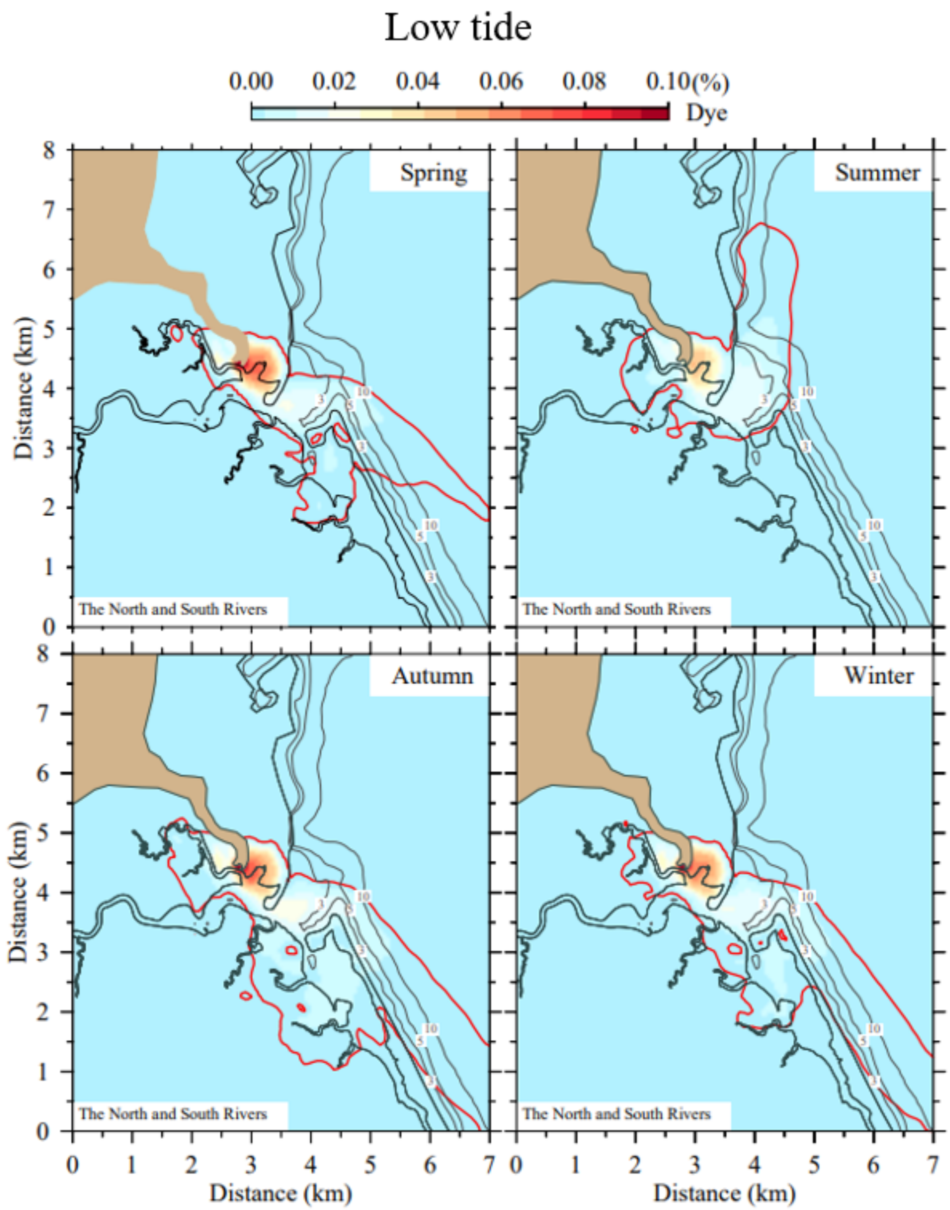

Fig. A14: Distributions of the WWTP effluents at low tide during the neap tidal period under seasonal-mean WWT discharge conditions in spring, summer, autumn, and winter for the case with the 50-year storm winds.

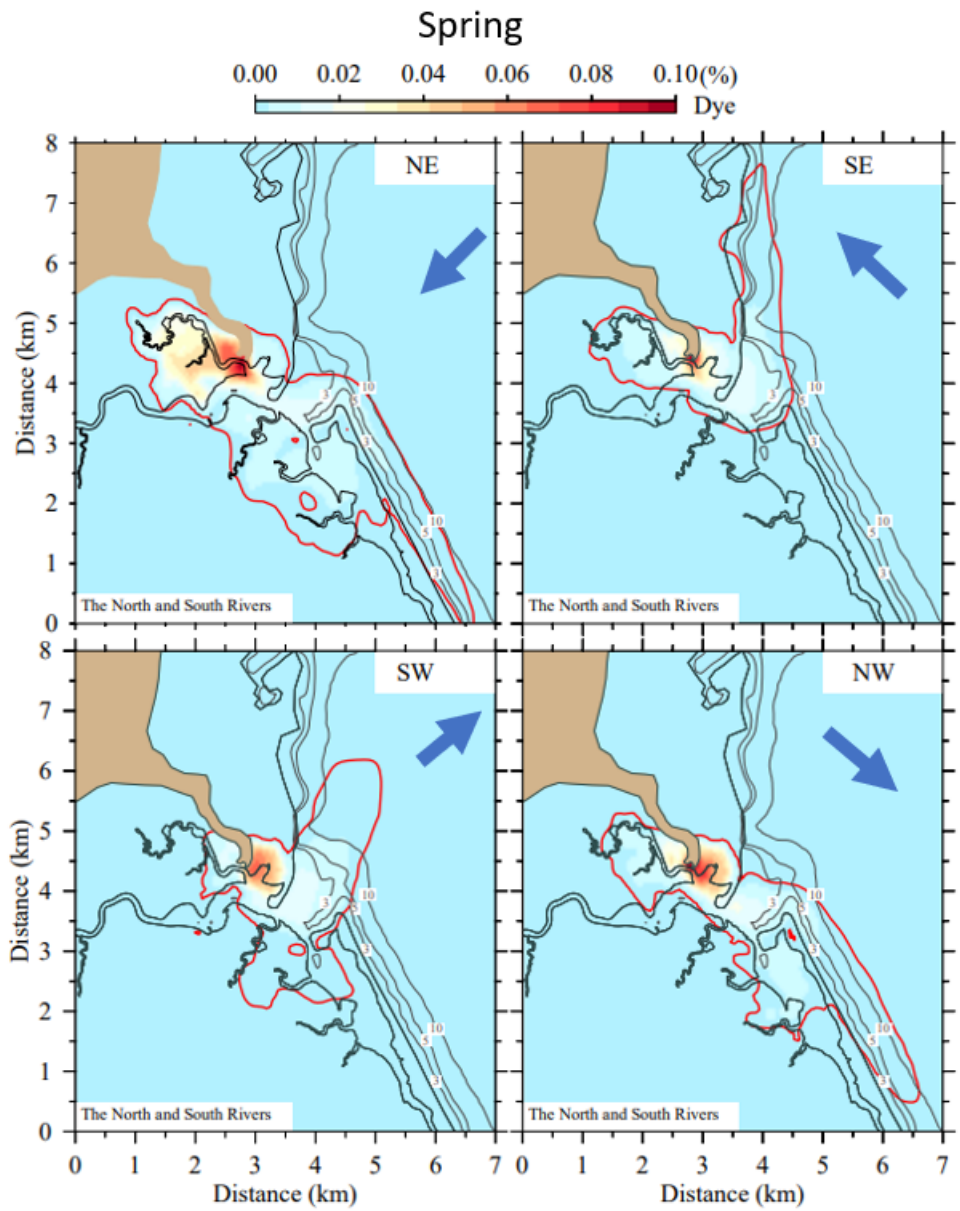

Fig. A15: Distributions of the WWTP effluents at high tide during the spring tidal period under northeasterly (NE), southeasterly (SE), southwesterly (SW), and northwesterly wind conditions. The model was run with seasonal-mean WWTP discharge in spring under a 50-year storm wind condition for spring. Arrows indicate the wind directions.

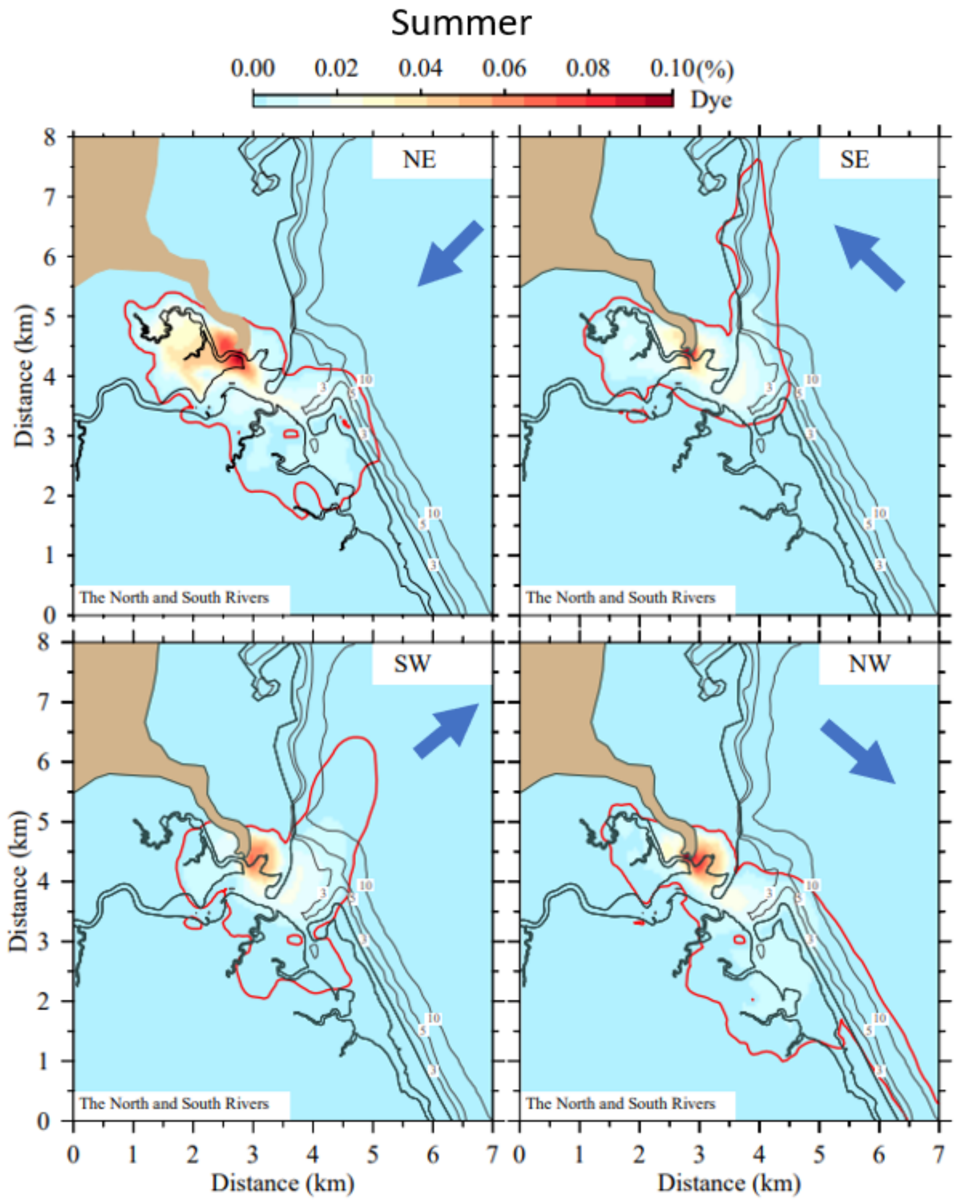

Fig. A16: Distributions of the WWTP effluents at high tide during the spring tidal period under northeasterly (NE), southeasterly (SE), southwesterly (SW), and northwesterly wind conditions. The model was run with seasonal-mean WWTP discharge in spring under a 50-year storm wind condition for summer. Arrows indicate the wind directions.

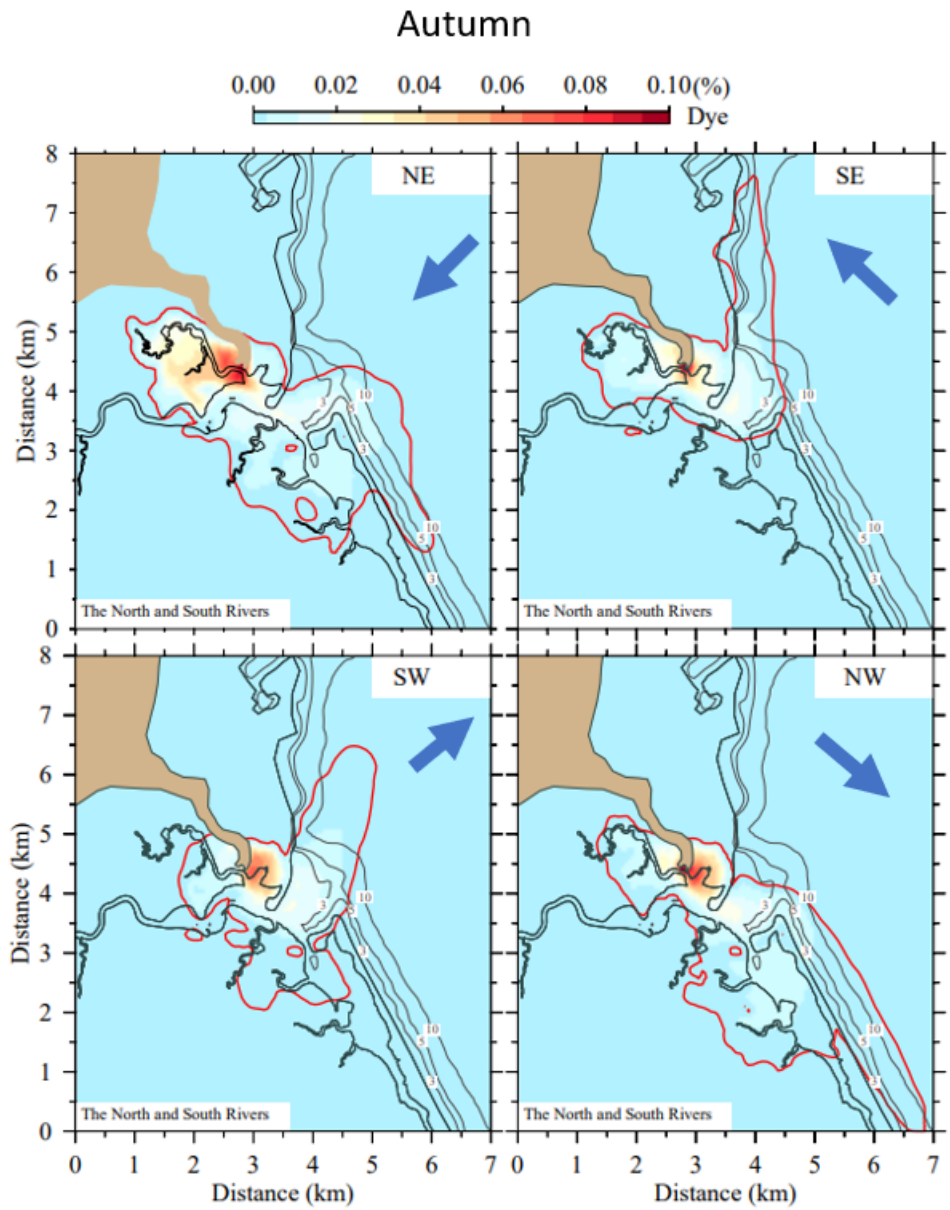

Fig. A17: Distributions of the WWTP effluents at high tide during the spring tidal period under northeasterly (NE), southeasterly (SE), southwesterly (SW), and northwesterly wind conditions. The model was run with seasonal-mean WWTP discharge in spring under a 50-year storm wind condition for autumn. Arrows indicate the wind directions.

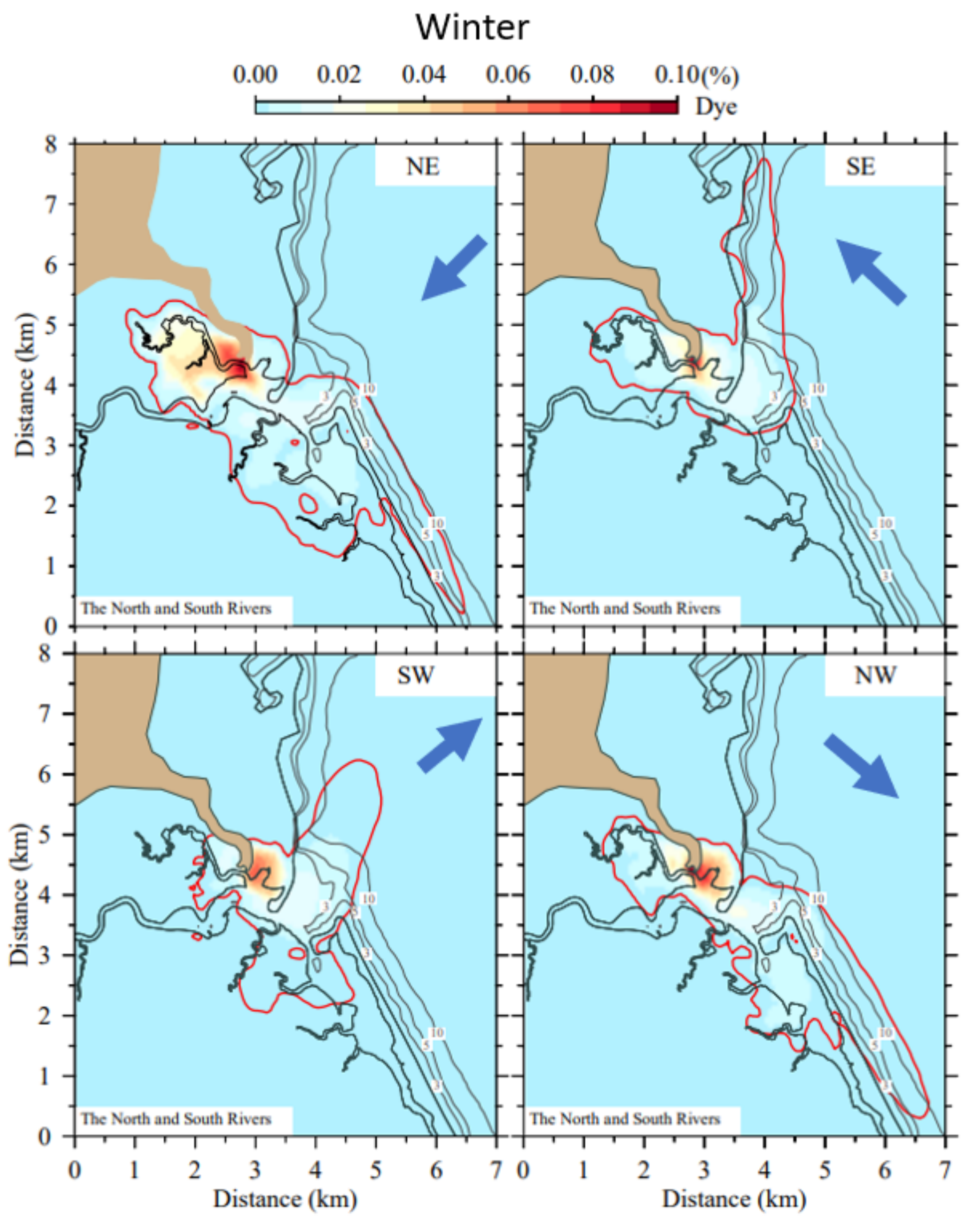

Fig. A18: Distributions of the WWTP effluents at high tide during the spring tidal period under northeasterly (NE), southeasterly (SE), southwesterly (SW), and northwesterly wind conditions. The model was run with seasonal-mean WWTP discharge in spring under a 50-year storm wind condition for winter. Arrows indicate the wind directions.

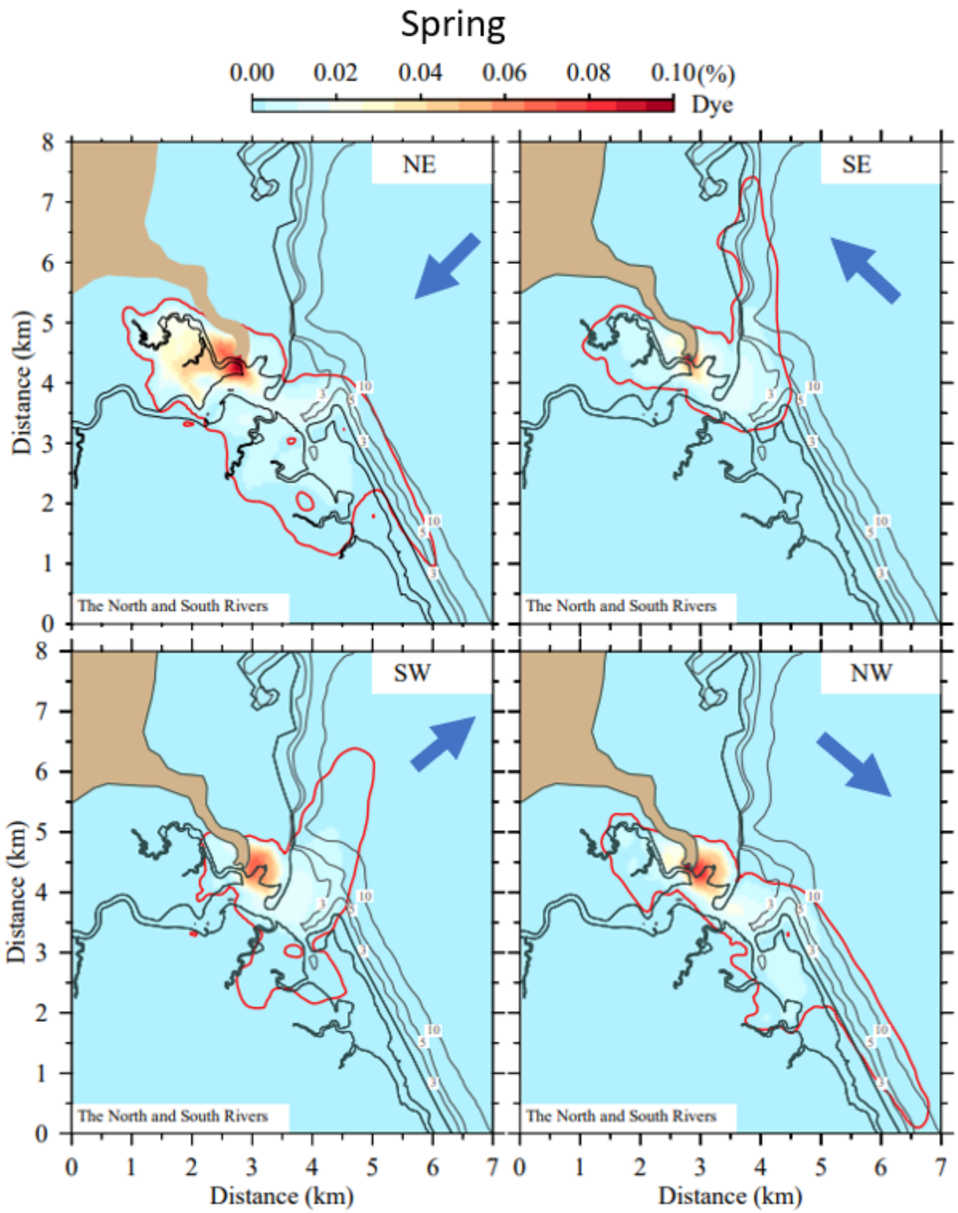

Fig. A19: Distributions of the WWTP effluents at high tide during the spring tidal period under northeasterly (NE), southeasterly (SE), southwesterly (SW), and northwesterly wind conditions. The model was run with seasonal-mean WWTP discharge in spring under a 100-year storm wind condition for spring. Arrows indicate the wind directions.

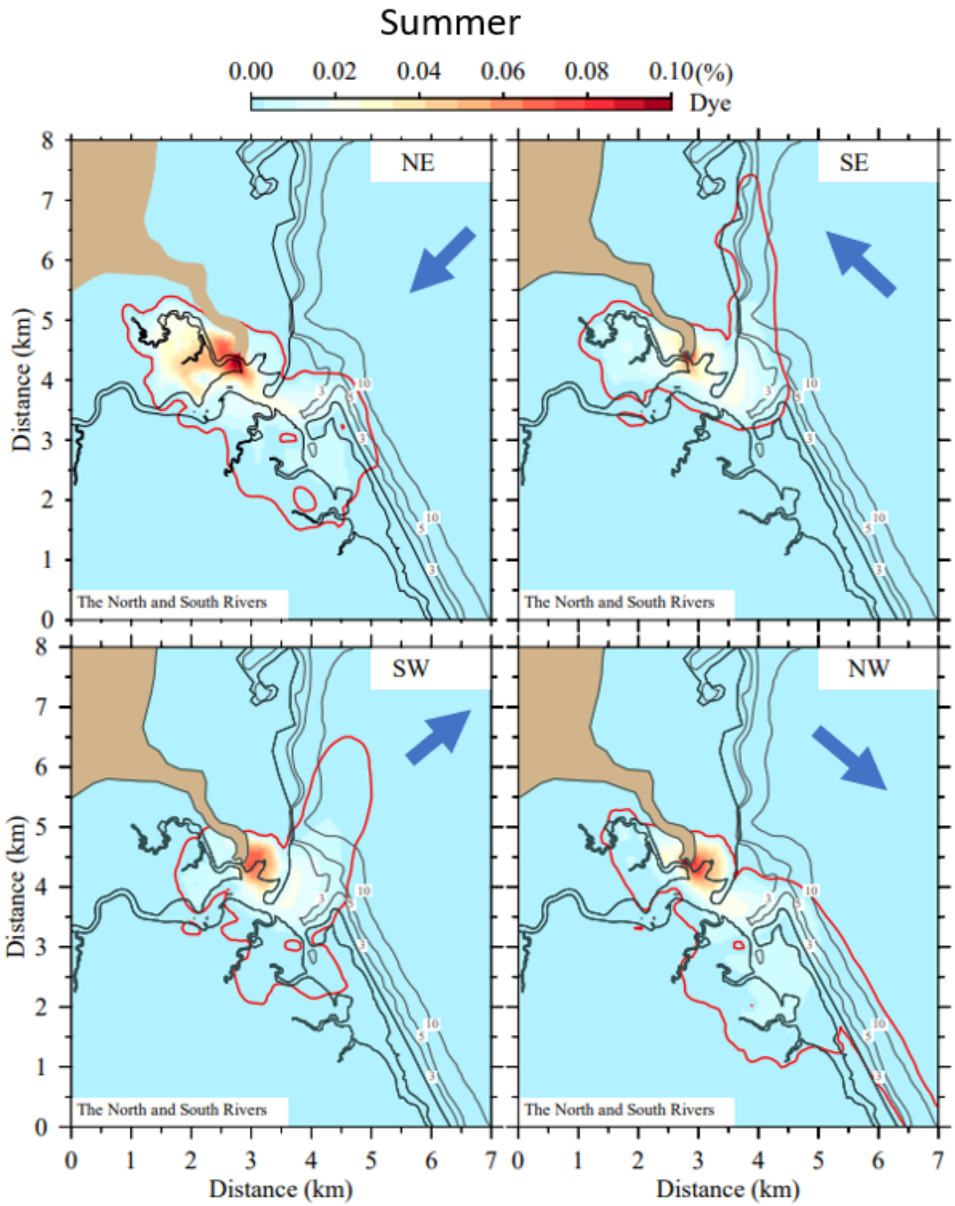

Fig. A20: Distributions of the WWTP effluents at high tide during the spring tidal period under northeasterly (NE), southeasterly (SE), southwesterly (SW), and northwesterly wind conditions. The model was run with seasonal-mean WWTP discharge in spring under a 100-year storm wind condition for summer. Arrows indicate the wind directions.

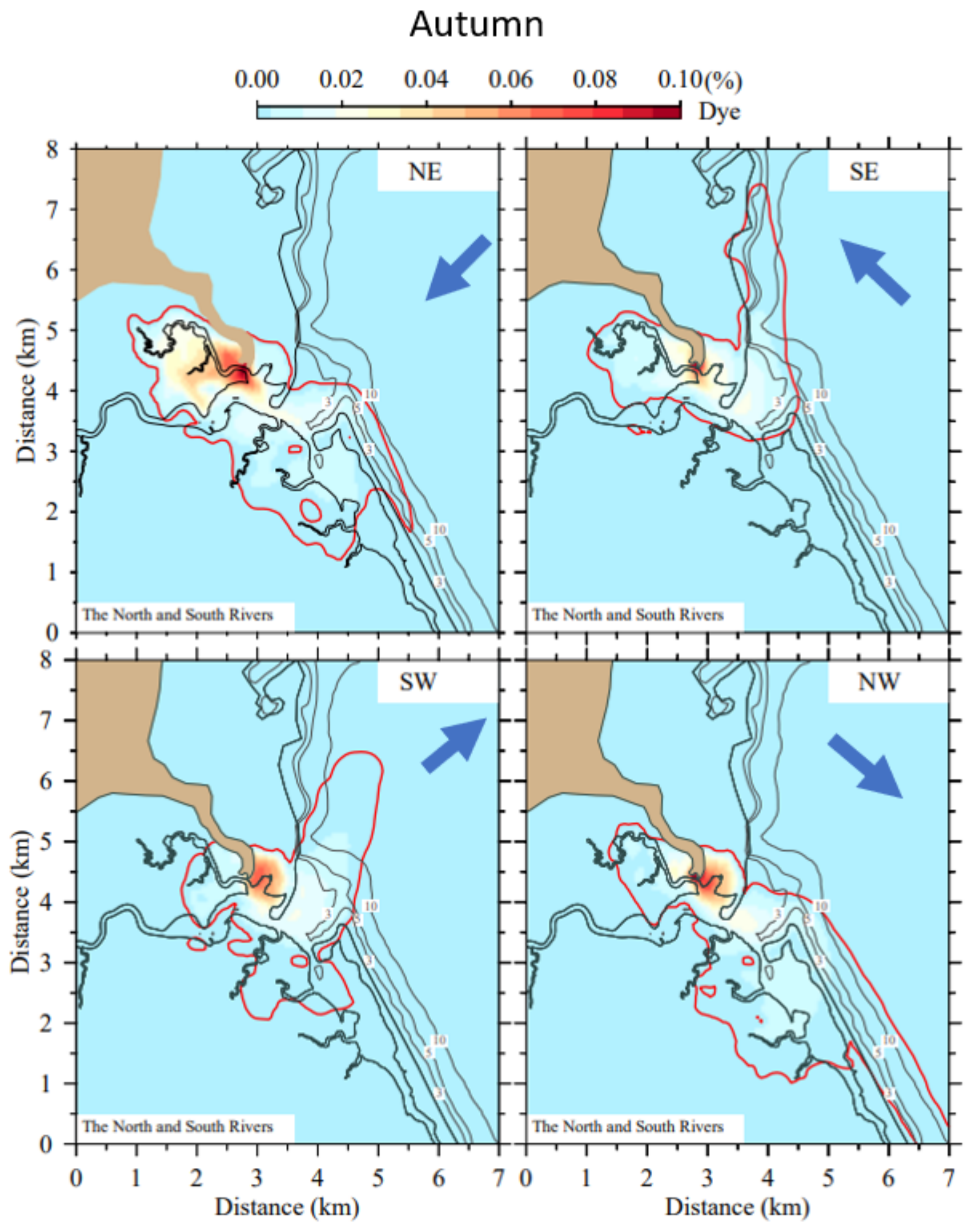

Fig. A21: Distributions of the WWTP effluents at high tide during the spring tidal period under northeasterly (NE), southeasterly (SE), southwesterly (SW), and northwesterly wind conditions. The model was run with seasonal-mean WWTP discharge in spring under a 100-year storm wind condition for autumn. Arrows indicate the wind directions.

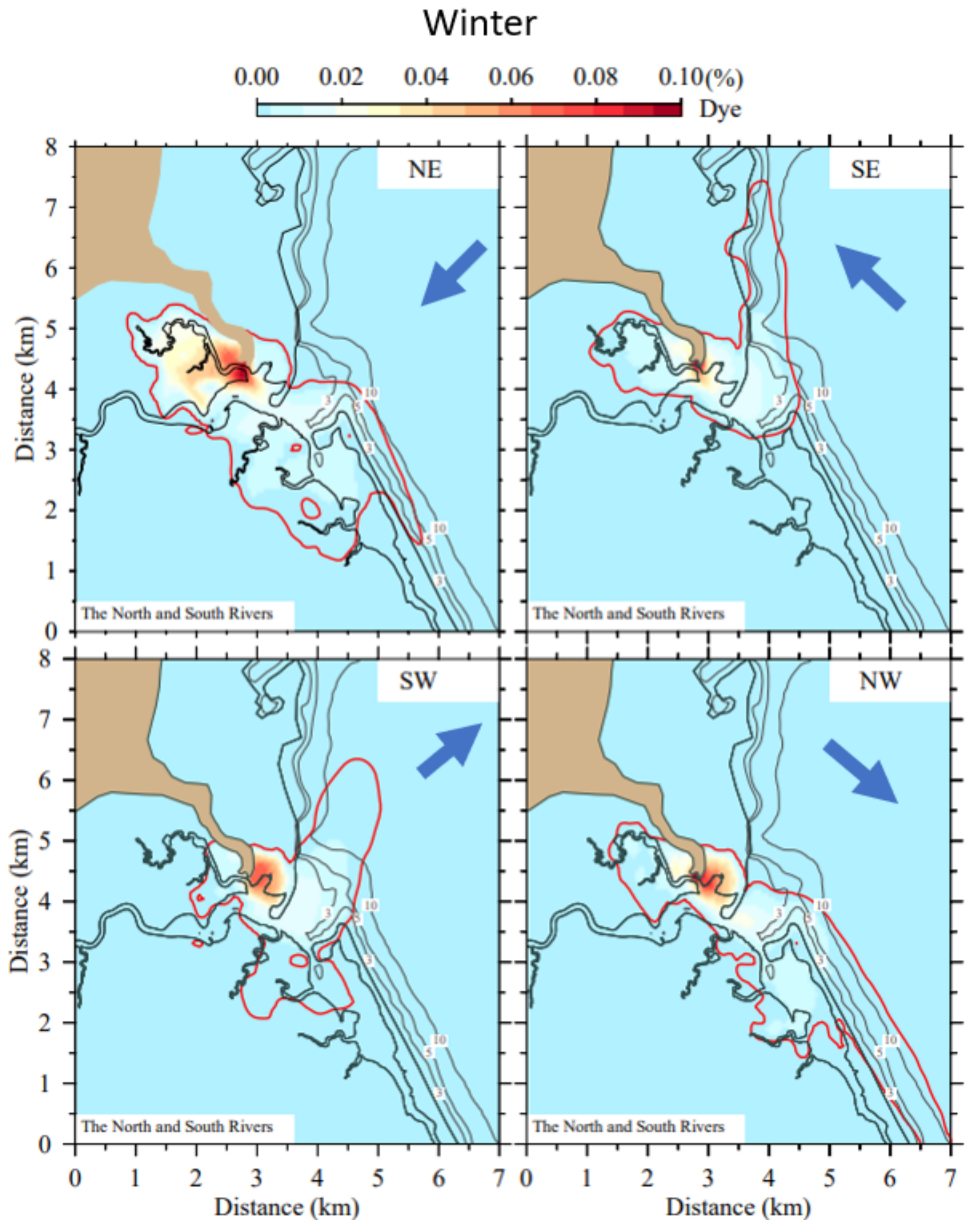

Fig. A22: Distributions of the WWTP effluents at high tide during the spring tidal period under northeasterly (NE), southeasterly (SE), southwesterly (SW), and northwesterly wind conditions. The model was run with seasonal-mean WWTP discharge in spring under a 100-year storm wind condition for winter. Arrows indicate the wind directions.

Appendix B: The spreading areas of WWTP effluents for the cases under seasonally-mean, 25, 50, and 100-year storm wind conditions

This appendix includes tables showing the spreading areas bounded by the 1000:1 dilution contour for the cases under seasonally-mean, 25, 50, and 100-year storm wind conditions.

Table B1: The spreading areas bounded by the 1000:1 dilution contour for the cases under seasonally-mean, 25, 50, and 100-year storm wind condition with the seasonal-mean WWTP effluents: Total: the total coverage area; inside: the coverage area in the estuary bordered by the New Inlet exit to the shelf; %: the percentage of the inside to the total; HH: high tide during the spring tide period; HL: low tide during the spring tide period ; LH: high tide during the neap tide period; LL: low tide during the neap tide period

Cases	Tide stages	Spring			Summer			Autumn			Winter		
		Total (km^2)	Inside (km^2)	%	Total (km^2)	Inside (km^2)	%	Total (km^2)	Inside (km^2)	%	Total (km^2)	Inside (km^2)	%
Seasonally-mean	HH	3.06	3.04	99.35	13.33	3.67	27.53	6.99	3.87	55.36	3.73	3.41	91.42
	HL	10.89	3.38	31.04	13.35	4.49	33.63	10.95	5.02	45.84	11.61	3.94	33.94
	LH	5.00	3.57	71.40	10.93	4.52	41.35	8.24	4.96	60.19	7.91	4.12	52.09
	LL	5.41	3.61	66.73	8.08	4.41	54.58	8.09	4.86	60.07	6.38	4.14	64.89
25-y storm	HH	4.23	4.22	99.76	3.85	3.28	85.19	5.44	5.43	99.82	4.76	4.75	99.79
	HL	8.08	3.55	43.94	7.74	2.94	37.98	11.30	6.01	53.19	9.12	4.50	49.34
	LH	3.77	2.45	64.99	4.68	2.61	55.77	5.98	4.75	79.43	4.12	3.05	74.03
	LL	4.92	2.23	45.33	5.47	2.52	46.07	8.68	4.51	51.96	6.08	2.83	46.55
50-y storm	HH	4.24	4.22	99.53	3.97	2.93	73.80	6.14	5.53	90.07	6.93	4.87	70.27
	HL	8.01	3.32	41.45	7.01	2.13	30.39	11.78	6.04	51.27	10.02	4.35	43.41
	LH	3.64	2.24	61.54	4.18	1.74	41.63	7.20	5.30	73.61	5.22	2.97	56.90
	LL	4.95	2.03	41.01	4.81	1.72	35.76	9.89	5.04	50.96	7.50	2.80	37.33
100-y storm	HH	4.27	4.26	99.77	3.43	2.82	82.22	6.96	5.63	80.89	5.90	4.62	78.31
	HL	8.14	3.29	40.42	7.35	2.08	28.30	11.94	5.99	50.17	9.85	3.78	38.38
	LH	3.52	2.12	60.23	3.79	1.87	49.34	6.92	4.79	69.22	5.04	2.64	52.38
	LL	5.02	1.95	38.84	4.45	1.84	41.35	9.63	4.62	47.98	7.27	2.48	34.11

Table B2: The spreading areas bounded by the 1000:1 dilution contour for the cases under seasonally-mean, and 100-year storm wind condition with the seasonal-maximum WWTP effluents: Total: the total coverage area; inside: the coverage area in the estuary bordered by the New Inlet exit to the shelf; %: the percentage of the inside to the total; HH: high tide during the spring tide period; HL: low tide during the spring tide period ; LH: high tide during the neap tide period; LL: low tide during the neap tide period

Cases	Tide stages	Spring			Summer			Autumn			Winter		
		Total (km^2)	Inside (km^2)	%	Total (km^2)	Inside (km^2)	%	Total (km^2)	Inside (km^2)	%	Total (km^2)	Inside (km^2)	%
Seasonally-mean	HH	4.25	3.58	84.24	12.36	3.88	31.39	8.03	4.15	51.68	5.03	3.72	73.96
	HL	10.97	3.52	32.09	10.26	4.42	43.08	10.34	5.25	50.77	10.83	3.81	35.18
	LH	7.62	3.57	46.85	8.11	4.36	53.76	9.11	4.93	54.12	7.90	3.82	48.35
	LL	5.94	3.57	60.10	8.03	4.28	53.30	8.65	4.93	56.99	6.35	3.83	60.31
100-y storm	HH	4.46	4.29	96.19	3.99	2.65	66.42	8.70	5.45	62.64	5.26	4.57	86.88
	HL	8.57	3.39	39.56	7.20	1.89	26.25	11.12	5.39	48.47	9.73	3.80	39.05
	LH	4.65	2.47	53.12	3.67	1.69	46.05	7.79	3.97	50.96	4.93	2.60	52.74
	LL	5.68	2.27	39.96	4.44	1.67	37.61	8.74	3.75	42.91	7.02	2.44	34.76

Table B3: The spreading areas bounded by the 1000:1 dilution contour at high tide during the spring tidal period for the cases under 25, 50, and 100-year storm wind condition with the seasonal-mean WWTP effluents: Total: the total coverage area; inside: the coverage area in the estuary bordered by the New Inlet exit to the shelf; %: the percentage of the inside to the total; NE: North-east wind; SE: South-east wind; SW: South-east wind; NW: North-west wind.

Cases	Wind direction	Spring			Summer			Autumn			Winter		
		Total (km^2)	Inside (km^2)	%	Total (km^2)	Inside (km^2)	%	Total (km^2)	Inside (km^2)	%	Total (km^2)	Inside (km^2)	%
25-y storm	NE	10.93	6.71	61.39	7.06	5.40	76.49	8.90	5.96	66.97	10.64	6.64	62.41
	SE	5.20	2.51	48.27	5.89	2.84	48.22	5.79	2.75	47.50	4.53	2.37	52.32
	SW	6.08	3.10	50.99	7.25	4.02	55.45	6.81	3.77	55.36	6.24	3.21	51.44
	NW	6.77	3.77	55.69	9.96	6.12	61.45	9.46	5.91	62.47	7.46	4.13	55.36
50-y storm	NE	9.50	6.63	69.79	6.74	5.67	84.12	7.82	6.07	77.62	9.16	6.56	71.62
	SE	5.49	2.65	48.27	5.93	2.95	49.75	5.67	2.84	50.09	5.76	2.70	46.88
	SW	5.86	2.84	48.46	6.77	3.63	53.62	6.68	3.49	52.25	5.86	2.98	50.85
	NW	6.70	3.42	51.04	9.77	5.84	59.77	9.51	5.75	60.46	7.22	3.81	52.77
100-y storm	NE	8.59	6.49	75.55	7.00	5.93	84.71	7.66	6.18	80.68	8.04	6.37	79.23
	SE	5.24	2.63	50.19	5.59	2.98	53.31	5.53	2.91	52.62	5.39	2.69	49.91
	SW	5.47	2.69	49.18	6.48	3.45	53.24	6.52	3.36	51.53	5.82	2.86	49.14
	NW	6.75	3.29	48.74	10.21	5.92	57.98	9.63	5.69	59.09	7.42	3.70	49.87

Table B4: The spreading areas bounded by the 1000:1 dilution contour at high tide during the spring tidal period for the cases under 25, 50, and 100-year storm wind condition with the seasonal-maximum WWTP effluents: Total: the total coverage area; inside: the coverage area in the estuary bordered by the New Inlet exit to the shelf; %: the percentage of the inside to the total; NE: North-east wind; SE: South-east wind; SW: South-east wind; NW: North-west wind.

Cases	Wind direction	Spring			Summer			Autumn			Winter		
		Total (km^2)	Inside (km^2)	%	Total (km^2)	Inside (km^2)	%	Total (km^2)	Inside (km^2)	%	Total (km^2)	Inside (km^2)	%
100-y storm	NE	8.81	6.61	75.03	7.28	6.16	84.62	8.01	6.35	79.28	8.34	6.50	77.94
	SE	3.85	2.12	55.06	4.24	2.51	59.20	4.17	2.44	58.51	3.91	2.18	55.75
	SW	5.64	2.70	47.87	7.27	3.47	47.73	7.19	3.39	47.15	6.01	2.80	46.59
	NW	7.81	3.11	39.82	10.53	5.43	51.57	10.43	5.23	50.14	8.82	3.62	41.04